



**Politecnico
di Torino**

Master of Science in Petroleum and Mining Engineering
A.a. 2021/2022

Master Thesis

**Impact of Relative Permeabilities on CO₂
Geological Storage**

Supervisor:

Prof. Francesca VERGA

Candidate:

Alain SAHLANI

Table of Contents

1	Introduction.....	1
2	CCUS Technical Overview	3
3	Trapping Mechanisms	6
3.1	Structural and Stratigraphic Trapping	7
3.2	Residual Trapping	8
3.3	Solubility Trapping	9
3.4	Ionic Trapping.....	10
3.5	Mineral Trapping	10
4	Relative Permeability and Capillary Pressure.....	12
4.1	Relative Permeability	12
4.2	Salt Precipitation.....	13
4.3	Capillary Pressure	14
4.3.1	Interfacial Tension and Capillary Pressure.....	14
4.3.2	Pc-kr-S Correlations.....	15
4.3.3	Hysteresis	17
4.4	Land Model	18
4.5	Snap-off.....	20
4.6	Capillary Pinning	21
4.7	Data Available in Literature.....	22
4.7.1	Steady State Tests	24
4.7.2	Unsteady Methods	25
4.7.3	Main Problems with Relative Permeability Measurements	26
5	Model and Simulation	28
5.1	Aquifer Model	28
5.1.1	Geochemical Model.....	29
5.1.2	Relative Permeability and Capillary Pressure	30
5.2	Sensitivity Analysis.....	31
6	Results and Discussions.....	34
6.1	Effect of Irreducible Water Saturation	34
6.2	Effect of the Endpoint of the Relative Permeability to CO ₂	38
6.3	Effect of the Land Coefficient	42
6.4	Effect of Capillary pressure.....	46

6.5	Effect of Corey Coefficient	51
7	Conclusion	56
8	References.....	58

List of Figures

Figure 1: The different trapping mechanisms and their storage security in function of the geologic timeline. [5] [13]	6
Figure 2: Structural and Stratigraphic trapping configuration: A)Anticline; B)Sealing fault; C) Stratigraphic pinchout; D) Unconformity [10]	7
Figure 3: Hydrodynamic trapping mechanism [10].....	8
Figure 4:Schematic showcasing the process of residual CO ₂ trapping. [14]	8
Figure 5:Convection currents of water due to dissolved CO ₂ [8].....	9
Figure 6:Variation of trapping type in function of pH and concentration of the formation cations [10].....	10
Figure 7:Schematic illustrating the different salt precipitation mechanisms [25]	13
Figure 8:a)Van Genutchen type capillary pressure b) is the Brooks-Corey type Pressure curve. [34]	15
Figure 9:Diagram showcasing a typical CO ₂ -brine relative permeability curves under the effect of hysteresis as well highlighting the distribution of CO ₂ between a free CO ₂ and trapped CO ₂ after a first imbibition [43]	19
Figure 10:Scheme showcasing the snap-off phenomenon leading to entrapment of the CO ₂ as non-connected bubbles. [44].....	20
Figure 11:Sketch representing the state of the CO ₂ plume after injection while focusing on highlighting capillary trapping at the trail of the plume. [44]	21
Figure 12: 3D representation of the aquifer model.....	28
Figure 13:CO ₂ injection history.....	29
Figure 14:Relative permeability to CO ₂ for different S_{wi}	34
Figure 15:Plot of the drainage and imbibition curves of CO ₂ for S_{wi} of 0.2 and 0.66	35
Figure 16: The distribution of the gas saturation at the end of the simulation (200years) for the base case (left) and $S_{wi} = 0.08$ (right).....	36
Figure 17: Distribution of gas saturation at the end of the simulation (200 years) for the base case (left) and $S_{wi} = 0.4$ (right).....	37
Figure 18: : Distribution of gas saturation at the end of the simulation (200 years) for the base case (left) and $S_{wi} = 0.66$ (right)	37
Figure 19:Relative permeability to CO ₂ for the different endpoints.....	38
Figure 20:Imbibition curves and Land model for a $k_{rCO_2}(S_{wi})=0.5$ (right) and the base case with $k_{rCO_2}(S_{wi})=0.8$ (left).	39
Figure 21: Imbibition curves and Land model for a $k_{rCO_2}(S_{wi})=0.1$ (right) and the base case with $k_{rCO_2}(S_{wi})=0.8$ (left).	39
Figure 22: The distribution of the gas saturation at the end of the simulation (200years) for the base case($k_{rCO_2}(S_{wi})=0.8$) (left) and $k_{rCO_2}(S_{wi})=0.5$ (right).....	40
Figure 23: The distribution of the gas saturation at the end of the simulation (200years) for the base case($k_{rCO_2}(S_{wi})=0.8$) (left) and $k_{rCO_2}(S_{wi})=0.1$ (right)	41
Figure 24: The variation of dissolved CO ₂ in function of time for the Base case and for the case($k_{rCO_2}(S_{wi})=0.5$)	41
Figure 25: The variation of residually trapped CO ₂ in function of time for the Base case and for the case($k_{rCO_2}(S_{wi})=0.5$).....	42
Figure 26: The distribution of the gas saturation at the end of the simulation (200years) for the base case($C=1.25$) (left) and $C=0.17$ (right).....	44
Figure 27: The distribution of the gas saturation at the end of the simulation (200years) for the	

base case($C=1.25$) (left) and $C=3$ (right)	44
Figure 28: The distribution of the gas saturation at the end of the simulation (200years) for the base case($C=1.25$) (left) and $C=8$ (right).	45
Figure 29: The distribution of the gas saturation at the end of the simulation (200years) for the Base case(left) and the case where P_c was not included (right).	47
Figure 30:The distribution of the residually trapped saturation of CO_2 at the end of simulation time (200 years) for the Base case(left) and the case where P_c was not included (right).	47
Figure 31:Figure showcasing the distribution of the residually trapped CO_2 at the end of the simulation (200 years) for the base case (left) and for the case where no capillary pressure hysteresis was included (right)	48
Figure 32:Plot of the drainage and imbibition capillary pressure curves for the base case and the simulation where $P_c=8.27$ kPa.	49
Figure 33: The distribution of saturation of residually trapped CO_2 at the end of simulation time (200 years) for the Base case(left) and the simulation where $P_c=8.27$ kPa (right).	49
Figure 34: The CO_2 saturation at the end of the simulation (200 years) for the base case (left) and simulation where $P_c=8.27$ kPa (right)	50
Figure 35:Relative permeability to CO_2 for different Corey exponents.	51
Figure 36:Relative permeability to water for different Corey exponents.	52
Figure 37:The distribution of the gas saturation at the end of the simulation (200years) for the base case($m=4.4;n=4.6$) (left) and sim12 ($m=2.2;n=4.6$) (right).....	54
Figure 38:The distribution of the gas saturation at the end of the simulation (200years) for the base case($m=4.4;n=4.6$) (left) and sim14 ($m=4.4;n=2.3$) (right).....	54
Figure 39:The distribution of the gas saturation at the end of the simulation (200years) for the base case($m=4.4;n=4.6$) (left) and sim15 ($m=4.4;n=7$) (right).....	55
Figure 40:The distribution of the gas saturation at the end of the simulation (200years) for the base case($m=4.4;n=4.6$) (left) and sim13 ($m=9;n=4.6$) (right).....	55

List of Tables

Table 1: The different models that correlate P_c and saturation and k_r and saturation [35].....	16
Table 2: Relative permeability data present in literature.....	23
Table 3:Composition of the brine water	29
Table 4: Different values adopted to perform the sensitivity analysis.	32
Table 5: Distribution of CO_2 among the different trapping mechanism by varying irreducible water saturation.	34
Table 6: Distribution of CO_2 among the different trapping mechanism for the different endpoint of the relative permeability to CO_2	38
Table 7: Distribution of CO_2 among the different trapping mechanism for the simulation where $C=0.17,3,8$ and the base case.....	43
Table 8: Distribution of CO_2 among the different trapping mechanism for the different capillary pressure curves.....	46
Table 9: Distribution of CO_2 among the different trapping mechanism for the different Corey exponents.	52

Abstract:

Carbon Capture Utilization and Storage (CCUS) is considered an important technology that can abate and reduce the anthropogenic effects of CO₂. The technology mainly consists in capturing the CO₂ from high-intensity emission sources and transporting it either to be utilized again as a raw material or to be stored permanently in adequate deep geological formations. The storing formations can be aquifers, oil and gas reservoirs, and coal mines. However, due to the abundant presence of aquifers, they are considered the best storage option for CO₂. Once injected, the CO₂ is trapped by a combination of several trapping mechanisms: the CO₂ can be trapped structurally under the cap rock, residually due to the capillary forces acting on the plume, or it can be trapped in the aqueous or ionic phase due to its solubility in the formation water, which can eventually lead to the mineralization of the CO₂. All of these mechanisms are affected by the plume size, shape, rock and formation water properties, thermodynamic conditions, injection strategy and migration trajectory. The mechanisms largely responsible for CO₂ trapping when the fluid is injected into an aquifer are structural trapping, which prevents CO₂ to flow upward due to the presence of an impermeable layer, and residual trapping, by which CO₂ is trapped permanently in the formation. Residual trapping depends on relative permeability and capillary pressure. For this reason, a thorough investigation was performed to assess the impact of all the parameters that influence relative permeability and capillary pressure. The storage of CO₂ for different rock-fluid interaction properties – thus different relative permeability and capillary curves – was simulated by the aid of a commercial software (GEM by CMG). During the study, the parameters defining the relative permeability curves were varied, namely the end points and the shape of the curves. The results indicate that the hysteresis of the relative permeability curves, typically described through the Land model, is the most impactful on CO₂ storage residual trapping and, as a consequence, also on amount of CO₂ trapped by solubility. The variation of the endpoints and the shape of the relative permeability curves have also effects on the storage mechanisms, and the preferred conditions are low critical water saturation, low relative permeability to CO₂ and strong capillary forces.

1 Introduction

Paris Agreement in 2015 and the continuous increasing climate awareness among societies have paved the way for one particular molecule to reach the wall of fame, as every scientist, politician, journalist, and even individual with no strong scientific background has come to acknowledge its name and have a global idea about its maleficent effect. It's "CO₂", the most famous substance in the Greenhouse Gas family. The reason behind the fame of this particular molecule is its effect on the heating of our Planet as its presence in the atmosphere traps the heat from the sun, which is leading to an acceleration in the increase of the Earth's average temperature. As well, the long-term effect of CO₂ is another aspect that increases its importance with respect to other greenhouse gases, as CO₂ can stay for several decades in the air after being emitted. [1]

After highlighting the noxious effects of CO₂ on our planet, one might think that eliminating all sources of CO₂ emissions from our daily activities can be a straightforward solution to this complicated problem. However, in our complex developing world, things are not that simple, as our historic reliance on CO₂ emitting sources to achieve economic growth and enhance the standard of living is still strong and persisting. Nonetheless, a lot of work and efforts have been put to mitigate what climate scientists call a “climate disaster”, through shifting from traditional fossil fuel energy sources to low carbon-emitting alternative sources as well as increasing energy efficiency among the different energy systems and incentivizing recycle, reuse policies, etc. All the above-mentioned actions have had a positive effect in reducing emissions while maintaining a strong economic development, but according to the United Nations report [2], we are still far away from reaching our emissions goals set in the notorious Paris Agreement. In order to close the emissions gap, a negative emission technology known under the name of Carbon Capture Utilization and Storage (CCUS) presents itself as a complementary solution to the previously mentioned technologies. As a matter of fact, the IEA report mentions that CCUS is of high necessity if we ever want to achieve net-zero emissions by 2050, and according to the Stated Policy Scenario, CCUS is set to account for more than 15% of CO₂ emissions mitigation in 2050. [3]

Currently, only 40 Mt of CO₂ are being captured per year, but this number will tend to increase and reach 1.6 Gt of CO₂ per year in the year 2030 and then rise further to 7.6 Gt of CO₂ in 2050, according to the Net Zero Emission scenario. It is also forecasted that in the year 2050, 95% of the captured quantity (7.22Gt of CO₂) will be permanently stored in geological formations, for which the current estimates of global geological storage capacity are well above the needed capacity. [4]

2 CCUS Technical Overview

After highlighting the importance of the CCUS technology and its necessity in order to reach carbon neutrality, now this technology is presented from a technical point of view and its ways of implementation are described.

As a first step, the CO₂ must be captured, and this activity is mainly performed next to high concentration emitting sources such as coal or gas-powered power plants, and heavy industrial plants.

According to the IPCC report [5], there are mainly three approaches to capturing CO₂:

- Pre-combustion carbon capture is implemented before the combustion process through fuel gasification with oxygen ex: in a power plant with integrated gasification combined cycle (IGCC) technology.
- Post-combustion carbon capture is when CO₂ is separated from the flue gas of a fossil fuel combustion.
- Oxyfuel combustion is when the CO₂ is separated during the oxy-combustion process e.g. using an oxygen gas turbine.

To capture the CO₂ in the previously mentioned situations, several technologies are being implemented such as:

- Adsorption and Absorption based technologies
- Membrane separation
- Cryogenic
- Chemical looping

As well, CO₂ can be directly captured from the air through Direct Air Capture (DAC) technology. Currently, there are only two technologies that can directly capture CO₂ from the air: solid DAC and liquid DAC. [6] [7]

After the capture of CO₂, it must be compressed and transported by pipeline, ship, rail, or truck, either to be utilized again as a raw material to deliver various necessary products such as fuels, chemicals, and building materials or to be permanently stored underground into an adequate storage formation. [5] [3]

There are mainly three options for permanently storing CO₂ away from the atmosphere:

1. Terrestrial Sequestration:

It's the process of capturing CO₂ from the atmosphere and storing it in soils and vegetation through photosynthesis. [8]

2. Ocean Sequestration:

As oceans cover approximately 70% of Earth's surface, ocean storing qualifies as the largest possible sink for CO₂. [8] At a depth higher than 1 kilometer, CO₂ could be injected into the water column, as at this depth the water has a lower density than CO₂, thus the CO₂ will disperse and dissolve and eventually

become a part of the global carbon cycle. However, huge concerns rise due to the environmental impact of CO₂ on marine life, as experiments have shown that increased CO₂ concentration is harmful to marine organisms. The negative effects of CO₂ injection in the ocean can range from having reduced calcification, reproduction, and growth among marine life to having higher mortality rates. [5]

3. Geological Sequestration of CO₂:

According to the IPCC report [5], the geologic storage of CO₂ can be executed both onshore and offshore, and there are three major types of geologic settings in sedimentary basins in which CO₂ can be safely stored underground:

- a. deep saline aquifers
- b. depleted oil and gas reservoirs
- c. unminable coal beds

- a. As mentioned by the IPCC in their report [5], saline aquifers present themselves as the most advantageous option among the above-mentioned formations from a storage capacity point of view. As well, the fact that the aquifer is saline, thus inadequate for other usages such as industrial and agriculture, makes this option even more favorable.
- b. On the other hand, depleted oil and gas reservoirs, in other words, reservoirs that are currently classified uneconomical after being produced for a certain period of time, can be considered as a good potential for geological storage. This is based on the fact that the mentioned reservoirs have previously stored oil and gas for a significant time, which promotes them as a proven safe storage for the injected CO₂. In addition, these reservoir formations have been extensively studied and modeled, thus abundant data and numerical models exist, which will increase the confidence in the storage site and result in a much easier job for the CO₂ storing operator to model, plan and inject the CO₂ in the subsurface. Furthermore, these types of storage formations can offer the already present infrastructure and wells for the CO₂ injection activities to take place. [8] Moreover, CO₂ can also be injected into currently producing oil and gas reservoirs as a way to enhance production. In oil reservoirs, CO₂ injection can increase production by up to 23 % of the oil originally in place (OOIP). However, more than half of the injected CO₂ is recovered with the oil and reinjected again for cost reduction purposes, which lowers the attractiveness of CO₂ Enhanced Oil Recovery (EOR) as a storage solution for the greenhouse gas. [5]
- c. In the case of CO₂ injection in coal beds, the CO₂ may displace the methane, which will increase methane production. This has been proved at the Allison project in Canada where the injected CO₂ has increased methane production by 80%. Nonetheless, the trapping mechanisms in coal beds are different from other formations as the dominant mechanism is the adsorption/absorption of CO₂ on the coal surfaces. However, coal swells when CO₂ is adsorbed and/or absorbed, which will reduce the permeability and eventually lead to a reduction

of the injectivity, and that can act as a major setback for CO₂ injection in coal formations. [8] [5]

The sequestration of CO₂ is presumed by many to be in its infancy and born due to the climate urgency. Nevertheless, CO₂ injection in the subsurface, either for Enhanced Oil Recovery purposes or for permanent geological storage, is actually a mature and well-developed technology. In fact, the first CO₂ injection activity took place back in 1972 for Enhanced Oil Recovery purposes [9], while the first CO₂ injection with the aim of CO₂ sequestration dates back to 1990. [10]

For proper CO₂ underground storage activity, the CO₂ must be injected as a supercritical fluid having a pressure and temperature higher than the critical ones ($P_c=73.7$ bar and $T_c=31^\circ\text{C}$) which are typically reached at a depth of 800 m, and this is attractive since supercritical CO₂ have a liquid-like density and a gas-like viscosity. The high density of the supercritical CO₂ makes storing the CO₂ in the supercritical conditions the most efficient way for geologic storage, while the low viscosity makes it advantageous from an injection point of view. [11] [12] It is worth mentioning that CO₂ liquid-like density is still significantly lower than that of the formation brine. [12]

Once the CO₂ is injected underground, it is subject to different physical and chemical interactions that will determine the fate of the injected CO₂ in the given formation. However, the ultimate fate will be determined by the different trapping mechanisms that will act on the CO₂ to immobilize it. In the upcoming section, the diverse trapping mechanisms will be briefly discussed and explained.

3 Trapping Mechanisms

The trapping mechanisms that act on the CO₂ to immobilize it underground can be divided in five different types in the following way [10]:

1. Structural and Stratigraphic Trapping
2. Residual Trapping
3. Solubility Trapping
4. Ionic Trapping
5. Mineral Trapping

Each of the trapping mechanisms will be briefly explained in the following part.

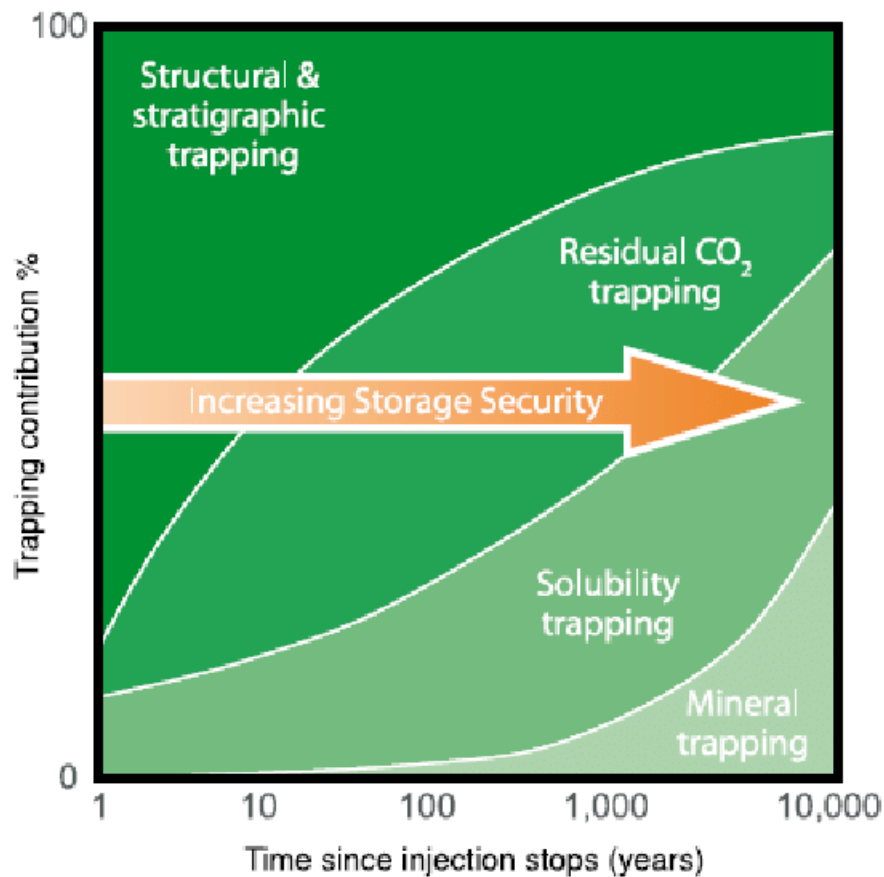


Figure 1: The different trapping mechanisms and their storage security in function of the geologic timeline. [5] [13]

3.1 Structural and Stratigraphic Trapping

At injection conditions, carbon dioxide is characterized by a density lower than the formation fluid, which will lead to an upward migration of the injected CO₂ due to the buoyancy effect. The upward migration will persist until the migrating CO₂ encounters a layer with low permeability or a high entry capillary pressure that will halt its upward movement and trap the gas in a structural trap. [8] [14] This type of trapping is in fact crucial for qualifying a given formation to be considered a storing site because the structural and stratigraphic trapping is the main mechanism that prevents CO₂ leakage through the top layer. [15]

The mentioned stratigraphic and structural traps are very similar to the ones discussed in an oil and gas context, and they include anticline folds, sealing faults, pinchout, and unconformity as illustrated in Fig.2. [14] [10]

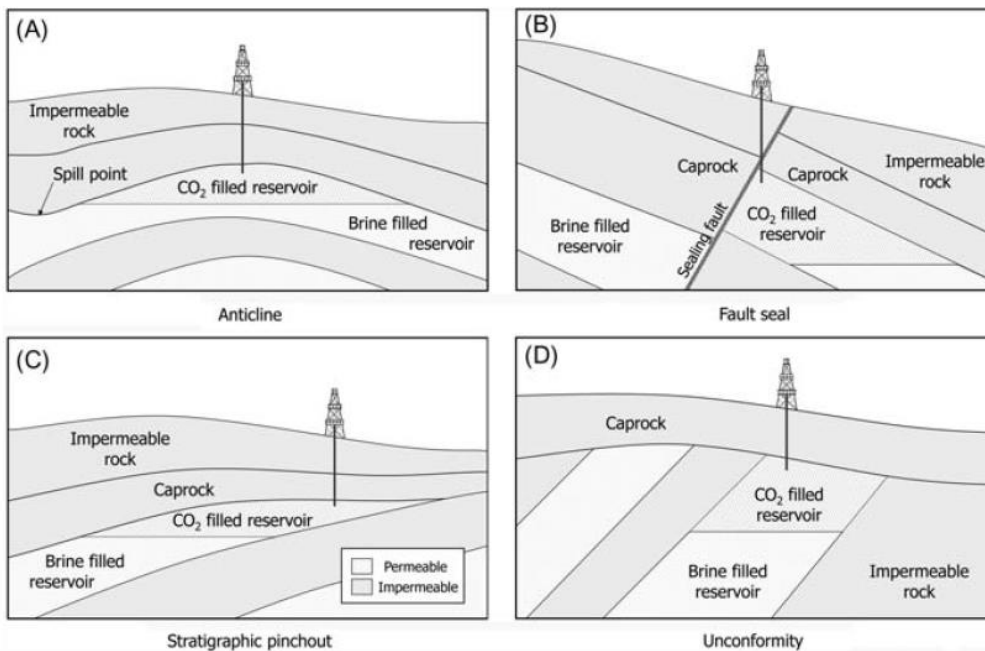


Figure 2: Structural and Stratigraphic trapping configuration: A)Anticline; B)Sealing fault; C) Stratigraphic pinchout; D) Unconformity [10]

As well, hydrodynamic trapping can occur in the case of an aquifer with a cap rock of very low dip angle or with a moderate dip angle but with the condition of counter-current hydrodynamic flow in order to hinder the upward flow of the plume, as illustrated in Fig.3. This trapping mechanism is only possible if the timescale for vertical ascension and reaching the surface is larger than the timescale for dissolution in the formation brine. [10]

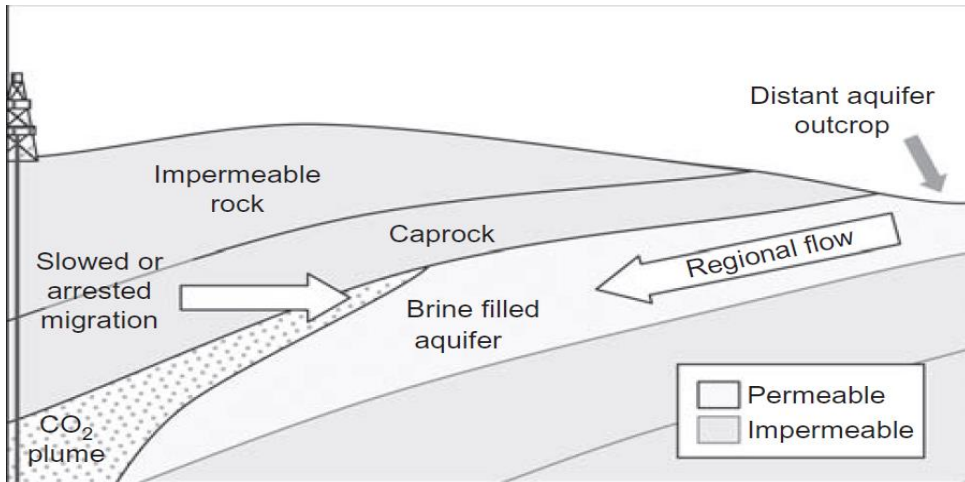


Figure 3: Hydrodynamic trapping mechanism [10]

3.2 Residual Trapping

As mentioned earlier, the CO₂ will migrate vertically due to buoyancy and will start to displace the water already present in the pores. During this buoyant ascension, imbibition (wetting phase displacing non-wetting phase) occurs as the water re-enters the pores invaded by the injected CO₂, and the tail of the rising CO₂ plume starts to be residually trapped by capillary forces. [16] This trapping mechanism has a big impact on the migration and fate of the CO₂ thus impacting other trapping mechanisms. [14] This type of trapping will be thoroughly discussed in the upcoming parts (4.5).

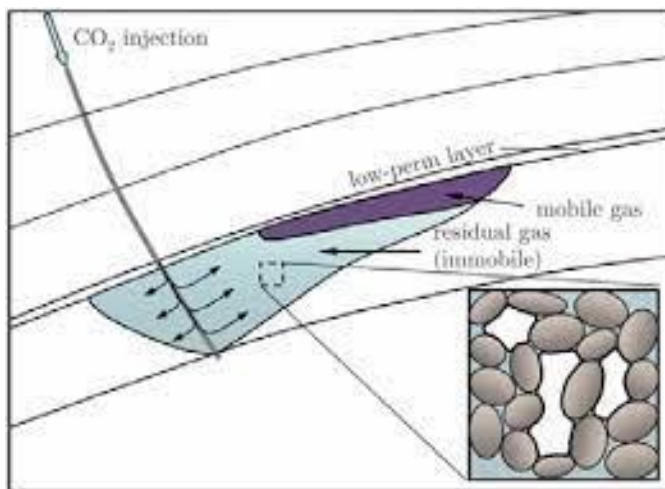


Figure 4: Schematic showcasing the process of residual CO₂ trapping. [14]

3.3 Solubility Trapping

CO₂ dissolution in the aquifer is an important long term trapping mechanism and is mainly controlled by CO₂ solubility in water. In its turn, the CO₂ solubility in water, is a function of pressure, temperature, pH, salinity and the chemical composition of the brine water. [10] As a matter of fact, the solubility of CO₂ decreases as salinity and/or temperature increase. [8]

As described earlier, the CO₂ upward movement is halted by the presence of a low permeability barrier. Once encountered that layer, the CO₂ plume will tend to spread laterally and will be in contact with the formation water. Then, a mass transfer phenomenon will occur and the CO₂ will start dissolving in the brine according to the molecular diffusion mechanism until an equilibrium state is reached. As the CO₂ gets dissolved in the water, the density of the aqueous solution slightly increases and flows downwards due to gravity forces. Then, it is replaced by the lighter and less saturated brine, which in its turn enhances the mass transfer phenomenon by increasing the concentration gradient and the mixing area due to the convection flow as shown in the figure 5. This process is slow due to the low diffusion coefficient, and it could take thousands of years for the CO₂ to become completely dissolved in the formation fluid. [14] [8]

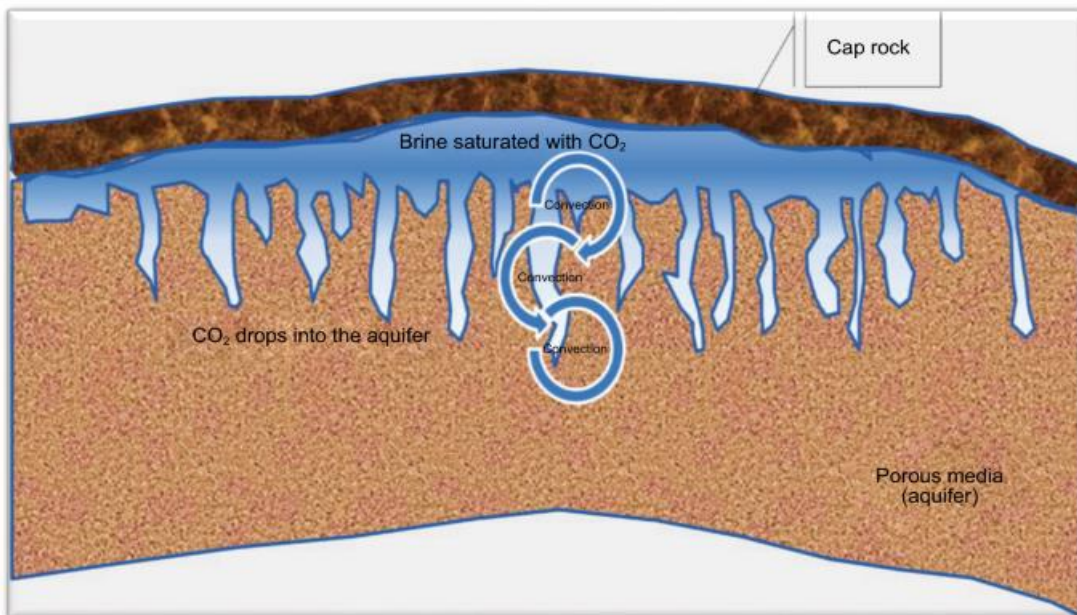
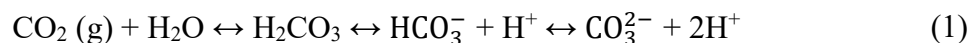


Figure 5: Convection currents of water due to dissolved CO₂ [8]

This trapping mechanism is highly beneficial as when the CO₂ dissolves in water, it no longer exists as a separate phase thus preventing it from leaking back to the surface. [5] [8]

The dissolution of CO₂ in formation waters can be represented by the following chemical reactions:



3.4 Ionic Trapping

Once the CO₂ dissolves in water, carbonic acid (H₂CO₃) is formed and then transformed into the bicarbonate ion(HCO₃⁻) and after that into carbonate ion CO₃²⁻ due to successive deprotonations, as described in Eq.1. Ionic trapping is mainly affected by pH as for pH higher than 6.3 (pKa1) the bicarbonate ion will be the predominate substance whereas for pH higher than 10.3(pKa2) the carbon will be in the form of carbonate ion. Therefore, ionic trapping will occur only if the pH is higher than ~ 6 as highlighted in Fig.6. It is also worth mentioning that both CO₂ dissolution and ionic trapping are considered as precursors for the mineral trapping mechanism. [10]

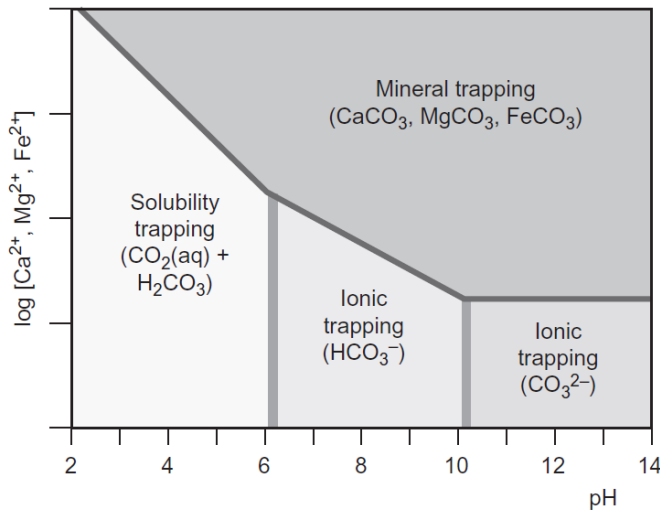


Figure 6:Variation of trapping type in function of pH and concentration of the formation cations [10]

3.5 Mineral Trapping

Mineral trapping is due to the interaction of CO₂ with the formation’s minerals, leading to its precipitation and incorporation in the mineral phase. While some reactions may be beneficial for the trapping and immobilization of CO₂, others may on the contrary facilitate its migration. [14]

As stated earlier, these reactions occur after CO₂ dissolution in water, which liberates a weak acid that reacts with the sodium and potassium basic silicate or calcium, magnesium and iron carbonate or silicate minerals in the reservoir formation to form bicarbonate ions. [5]

The acidity and salinity of the brine formation will be influenced by the presence of calcium, iron, or magnesium carbonate minerals in the rock matrix, which will be attacked by the weak acid. [17]



The typical mineral reactions resulting from the reaction of weak acid with aluminosilicate minerals present in clays and feldspars, include:

- Precipitation of calcite and kaolinite or dawsonite from the carbonation of albite:

$$2\text{NaAlSi}_3\text{O}_8 + \text{H}_2\text{CO}_3 + \text{H}_2\text{O} + \text{Ca}^{2+} \leftrightarrow 4\text{SiO}_2 + \text{CaCO}_3 + \text{Al}_2\text{Si}_2\text{O}_5(\text{OH})_4 + 2\text{Na}^+ \quad (3)$$



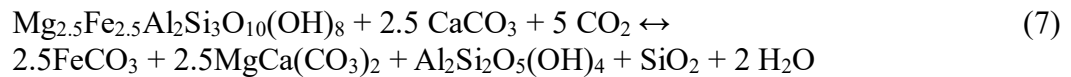
- Precipitation of calcite and kaolinite from the carbonation of anorthite:

$$\text{CaAl}_2(\text{SiO}_4)_2 + \text{CO}_2 + 2 \text{H}_2\text{O} \leftrightarrow \text{CaCO}_3 + \text{Al}_2\text{Si}_2\text{O}_5(\text{OH})_4 \quad (5)$$

- Precipitation of dawsonite from the carbonation of K-feldspar:

$$\text{KAlSi}_3\text{O}_8 + \text{CO}_2 + \text{H}_2\text{O} + \text{Na}^+ \leftrightarrow 3 \text{SiO}_2 + \text{NaAlCO}_3(\text{OH})_2 + \text{K}^+ \quad (6)$$

- Precipitation of siderite, dolomite, and kaolinite from the alteration of the clay mineral chlorite:



[10] [17]

Some reactions can be rapid (days) such as the reaction of CO₂ with some carbonate minerals, whereas others are slow (hundreds to thousands of years) as in the case of Silicate minerals. [5] In fact, as shown in Fig.1, this trapping mechanism is the slowest of them all and it will only become significant at geological time scale. [10] [14]

This was proved by the simulation study in this article [18], as they predicted that all the injected CO₂ in the Weyborn Oilfield will be trapped in the mineral form after 5000 years. The mineral trapping mechanism is dependent on several factors and properties such as the mineral composition of the rock, gas pressure and temperature, and porosity. [19] [8]

4 Relative Permeability and Capillary Pressure

After discussing the different trapping mechanisms, and seeing that they are all affected by the fate of the CO₂ in the aquifer so it is in our interest to study the effect of relative permeability of the CO₂ in the aquifer as it will depict the size and shape of the CO₂ plume in the formation. Equally important, the injectivity of CO₂ in the aquifer is strongly dependent on the mobility of the fluid in the subsurface. Thus investigating the relative permeability is of high importance for practical implementation of CO₂ storage projects in brine aquifers. [20] [21] [22] For these reasons, the remainder of the paper will be mainly focused on the CO₂-brine relative permeability curves in addition to the capillary pressure curves to study their effects on the total trapped CO₂ under the different mechanisms mentioned earlier.

4.1 Relative Permeability

The term relative permeability is used when we have a concurrent flow of multiple fluids in the porous media. In this case, the resistance to flow is increased by the presence of another fluid and it is known that the sum of the effective permeability of each fluid is less than the intrinsic permeability of the rock. By applying the Darcy's Law to each fluid i present in the porous media we can write:

$$q_i = -\frac{k_i}{\mu_i} \nabla \Phi_i \quad (8)$$

Here k_i is the effective permeability of phase i , Φ_i is the potential with components of pressure and gravitational potential of fluid i ($P_i + \rho_i g z$); where P_i [Pa] is the fluid pressure, ρ_i [kg/m³] is the fluid density, g 9.8 m/s² is the acceleration due to gravity, and z [m] is a spatial coordinate in the vertical direction (i.e. with or opposite to the direction of the gravitational force), and ∇ is the nabla operator. [21]

We know that k_{ri} , the relative permeability to phase i , is the ratio of the effective permeability k_i of the phase i to the absolute permeability k .

$$k_{ri} = \frac{k_i}{k} \quad (9)$$

Thus the previous equation (Eq.8) can be written as:

$$q_i = -\frac{k_{ri} k}{\mu_i} \nabla \Phi_i \quad (10)$$

The relative permeability to a phase i is said to be related to the saturation of that phase in a way that the relative permeability to that phase increases with its saturation ($k_{ri} = k_{ri}(S_i)$). [21] [23] Further correlations relating the relative permeability to the saturation will be presented in the following parts.

4.2 Salt Precipitation

Salt precipitation is one of the factors that can affect the injectivity of CO₂. The salt precipitation mechanism will be briefly discussed due to its effect on both the absolute permeability and the relative permeability to the CO₂. [24] [25]

Salt precipitation can be mainly attributed to physical processes rather than chemical processes as one might think. The several physical processes contributing to salt precipitation can be summarized as the following:

- 1) 2-phases displacement of brine away from the well
- 2) Brine evaporation into the CO₂ stream
- 3) Capillary backflow of the liquid phase towards the well due to capillary pressure gradients
- 4) Molecular diffusion of salt in the aqueous phase
- 5) Salt self-enhancing
- 6) Gravity override of injected CO₂

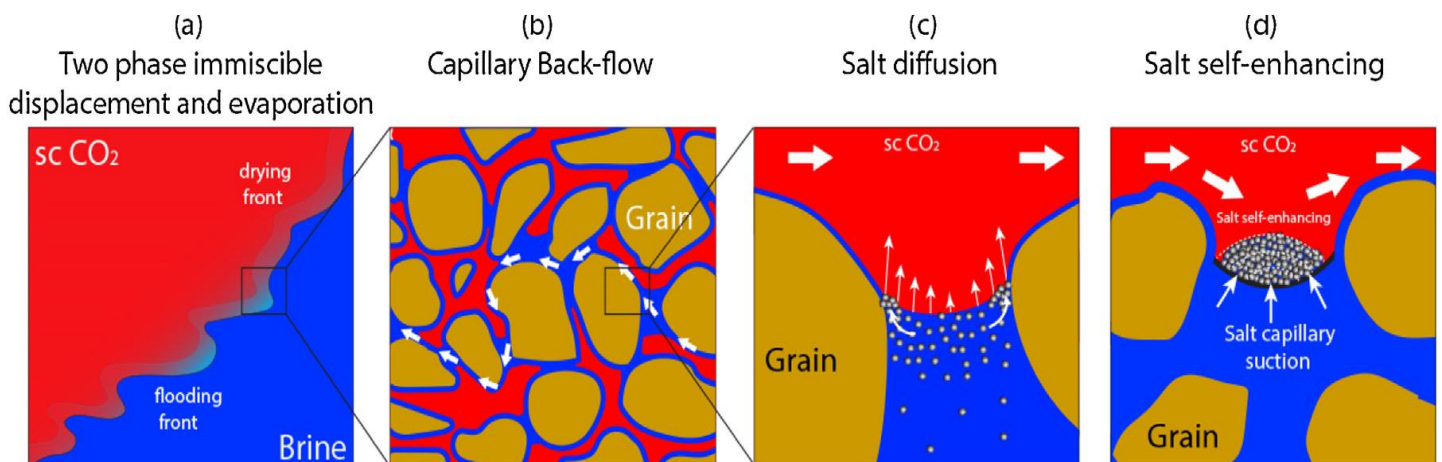


Figure 7: Schematic illustrating the different salt precipitation mechanisms [25]

The above-mentioned processes will be briefly discussed in the upcoming paragraph to form a first idea on salt precipitation.

The two-phase displacement process occurs during primary drainage as the injected CO₂ pushes the brine water out of the well. This will form a two-phase flow zone where both the aqueous phase and super critical CO₂ (scCO₂) coexist Fig.7(a). Simultaneously evaporation takes place in the drained region thanks to the low water vapor pressure of the trapped brine and the relatively high solubility of brine into CO₂ compared to the solubility of CO₂ into the brine, which is several orders of magnitude lower. [25] [26] The water evaporation will increase the permeability to CO₂, which will in its turn increase the spread of CO₂ and once again increase the evaporation of brine, thus creating a dry-out front. [27] [26] The water mass exchange mainly occurs in the dry-out zone resulting in a saturation gradient across the drying front, which is higher than the one created in pure viscous displacement. This will

lead to a capillary pressure gradient that will eventually overcome the injection pressure gradient and push back the water towards the evaporation front, thus supporting more evaporation. [25] As evaporation continues, the salt will ultimately reach the solubility limit and will initiate precipitation out of the solution. [24] [26] In fact, salt has a strong affinity towards water enabling it to imbibe brine from long distances towards the evaporation front, which will result in further precipitation. [25] [27]

However, for the remainder of this paper, the study of salt precipitation near the wellbore area will be left out.

4.3 Capillary Pressure

4.3.1 Interfacial Tension and Capillary Pressure

The mechanical equilibrium between two fluids in the reservoir is not only governed by hydrostatic and gravity action but also by capillary action. The latter is the result of a fluid-fluid and fluid-rock interactions. The interface of two phases has an associated energy per unit of surface area and this is due to the configuration of molecules at the interface. The interfacial tension $\gamma_{i,j}$ [mN/m] is adopted to describe the energy inherent at the interface between phase i and phase j . This energy is responsible for the pressure difference present at the interface of two fluid immiscible fluids (i.e. capillary pressure). In fact, capillary pressure can be related to the interfacial tension by the Young-Laplace equation:

$$P_c = P_{nw} - P_w = \frac{2 \gamma_{b,CO_2} \cos\theta}{R} \quad (11)$$

Where P_{nw} is the phase pressure of the non-wetting phase, P_w is the phase pressure of the wetting phase, γ_{b,CO_2} is the brine-CO₂ interfacial tension, R is the largest connected pore radius and θ is the contact angle, which is related to reservoir wettability. [28] [29] [21]

It has been found by [30] that the interfacial tension (IFT) of a CO₂/brine system at conditions relevant to subsurface storage is in the range of 20-55 mN/m, with most systems being water wet. Although IFT is considered an important parameter to control during enhanced oil recovery as it affects the oil residual saturation, it was found by [22] that in the above-mentioned range, IFT has no important effect on the relative permeability curves in the CO₂ sequestration context.

Capillary pressure can also be described as the amount of pressure required so that the non-wetting phase can displace the wetting phase. As a result, in a porous media context, the non-wetting phase can displace the wetting phase only if the pressure applied is at least equal to the capillary pressure of the largest pore. [31]

The two most important and the most widely used models for capillary pressure curves are the Van Genuchten (VG) model [32], which relates the capillary pressure to the saturation with an S-shaped curve, and the Brooks-Corey (BC) model [33], which on the other hand represents the relation with a convex-shaped curve. The difference between the two models

is not limited to the curve's shape but also in defining the entry capillary pressure. While Brooks model defines the entry capillary by a non-zero plateau value, Van Genuchten uses a steep slope to link the endpoint (P_c at S_w equal to 1), which is usually zero, to the plateau region as indicated in Fig.8. [34]

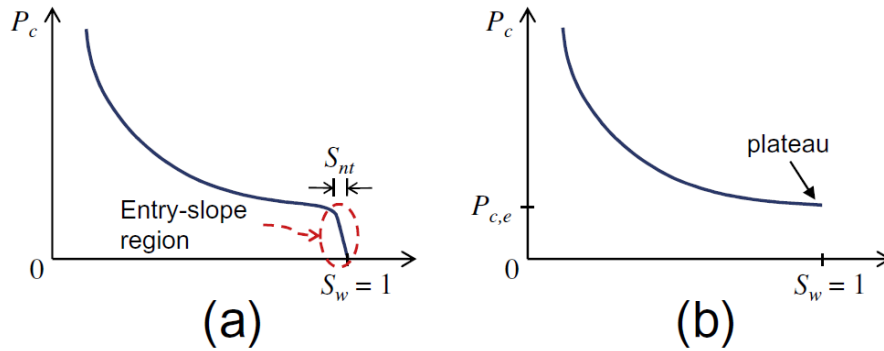


Figure 8:a)Van Genuchten type capillary pressure b) is the Brooks-Corey type Pressure curve. [34]

4.3.2 P_c - k_r - S Correlations

It has been reported in literature several ways to represent the capillary pressure and relative permeability curves in function of saturation.

The different correlations and models are presented in table 1.

Table 1: The different models that correlate P_c and saturation and k_r and saturation [35]

Model	P_c	k_r
Van Genuchten-Mualem	$S_l^*=(1+\alpha P_c^{nv})^{-mv}$	For $S_l > S_{li}$: $k_{rl} = S_l^{*1/2} [1-(1- S_l^{*1/mv})^{mv}]^2$ $k_{rg} = S_g^{*1/2} [(1- S_l^{*1/mv})^{mv}]^2$ For $S_l < S_{li}$: $k_{rg}=1$; $k_{rl}=0$
Brooks-Corey-Burdine	$S_l^*=(P_c/P_e)^{-\lambda}$	For $S_l > S_{li}$: $k_{rl} = S_l^{*(3+2\lambda)}$ $k_{rg} = S_g^{*2} [1- S_l^{*(1+2/\lambda)}]$ For $S_l < S_{li}$: $k_{rg}=1$; $k_{rl}=0$
Van Genuchten-Corey	$S_l^*=(1+\alpha P_c^{nv})^{-mv}$	For $S_l < S_{li}$: $k_{rg}=1$; $k_{rl}=0$ For $S_l > S_{li}$: $k_{rl} = S_l^{*4}$ $k_{rg} = S_g^{*2} [1- S_l^{*2}]$
Van Genuchten –Hybrid-Mualem -Corey	$S_l^*=(1+\alpha P_c^{nv})^{-mv}$	For $S_l > S_{li}$: $k_{rl} = S_l^{*1/2} [1-(1- S_l^{*1/mv})^{mv}]^2$ $k_{rg} = S_g^{*2} [1- S_l^{*2}]$ For $S_l < S_{li}$: $k_{rg}=1$; $k_{rl}=0$
Van Genuchten - Endpoint Power Law	$S_l^*=(1+\alpha P_c^{nv})^{-mv}$	For $S_l > S_{l0}$: $k_{rl} = k_{rl0-EPL} \left(\frac{S_l - S_{l0}}{1 - S_{l0}} \right)^{N_{l0-EPL}}$ $k_{rg} = k_{rg0-EPL} \left(\frac{S_g}{1 - S_{l0}} \right)^{N_{g-EPL}}$ For $S_l < S_{l0}$: $k_{rl}=0$ $k_{rg} = 1 - \left(\frac{1 - k_{rg0-EPL}}{S_{l0}} \right) S_l$
Brooks-Corey-Variable Corey	$S_l^*=(P_c/P_e)^{-\lambda}$	$k_{rl} = S_l^{*N_{l-VC}}$ $k_{rg} = k_{rg0-VC} S_g^{*2} [1- S_l^{*N_{l-VC}}]$ For $S_l < S_{li}$: $k_{rg}=1$; $k_{rl}=0$

Where:

$$S_l^* = \frac{S_l - S_{li}}{1 - S_{li}}$$

$$S_g^* = \frac{S_g}{1 - S_{li}}$$

$P_c = P_g - P_l$ (P_g =pressure of the gas phase, P_l =pressure of the liquid phase)

α is the Van Genuchten parameter (1/Pa)

λ Brooks-Corey pore geometry factor

k_{rj} relative permeability of phase j

nv and mv Van Genuchten shape parameter, and mv is also defined as: $mv=(1-1/nv)$

N_{j-CV} coefficient for variable Corey relative permeability model (phase j)

N_{j-EPL} coefficient for variable Endpoint power law relative permeability model (phase j)

P_e Brooks-Corey entry pressure (Pa)

P_c capillary pressure (Pa)

S_j phase j saturation

S_{li} aqueous irreducible saturation
 S_{l0} aqueous endpoint saturation
[35]

The Van Genuchten-Mualem (VG-M) has been rarely used, and it's a coupled S- P_c - k_r model with the same pore geometry parameter m_v in both S- P_c and S- k_r relations. Similarly, the Brooks-Corey-Burdine (BC-B) model is mostly implemented as a coupled S- P_c - k_r model but with λ as the pore geometry parameter. Conversely, the Van Genuchten-Corey (VG-C) is an uncoupled approach where the k_r -S relations are only related to the effective water saturation and do not depend on any sediment property. The hybrid approach in the Van Genuchten – Hybrid-Mualem -Corey (VG-hMC) model uses the Mualem k_{rl} -S relations that are usually coupled to the VG S- P_c relations through the m_v parameter and it uses the uncoupled k_{rg} – S relation of Corey. Regarding the Van Genuchten - Endpoint Power Law (VG-EPL) model, its application comes with a complication due to the fact that S_{l0} , the saturation at which the highest relative permeability to gas is obtained experimentally, which is usually higher than the irreducible water saturation S_{li} in the VG S- P_c equations. The last model consists in using fitted k_r -S relations. The variable Corey exponents are varied to enable the inclusion of fitted gas relative permeability beyond the experimentally obtained endpoint gas saturation. [35]

4.3.3 Hysteresis

Since both, relative permeability and capillary pressure curves are subject to hysteresis, this phenomenon will be briefly explained.

Hysteresis is by definition the dependence of a state of a system on its history and on the direction of evolution, which creates irreversibility. In the context of this work, this phenomenon is present in the relative permeability and capillary pressure as we don't have a one-to-one correspondence between saturation and relative permeability or capillary pressure. [36] [37] First, let's define imbibition as the process in which displacement results in an increase in the wetting phase saturation. On the other hand, drainage will be defined as the process resulting in an increase in the non-wetting phase saturation (a decrease in the wetting phase saturation). [21]

At least two phenomena have been identified as the source of hysteresis. The first one is having a contact angle hysteresis: it occurs when the contact angle of the wetting phase displacing the non-wetting phase is higher than the receding angle when the wetting phase is being displaced by the non-wetting phase. The second source is when a fraction of the non-wetting phase gets disconnected and trapped during an imbibition process. [36] [38] [37]

In the case of relative permeability curves, we can observe hysteresis as the drainage and imbibition curves generally differ. During the imbibition phase, one of the consequences of hysteresis is that the relative permeability to the non-wetting phase can reach zero without the necessity that the saturation of the non-wetting phase reaches zero. In fact, a significant fraction of the non-wetting phase will be remained trapped in the pores, which we define as irreducible or residual saturation. [21] [22] As well, it has been observed that the non-wetting

phase experiences stronger hysteresis with respect to the wetting phase. [37]
 The effect of hysteresis is magnified in situations of strong flow reversals such as alternating/cyclic water-gas injection, which will result in the trapping of the gas by water. [36]
 In the context of CO₂ injection into a brine aquifer, the drainage process occurs when the injection starts as the CO₂ starts to displace the water and pushes it away from the injection well. Meanwhile, an imbibition process takes place at the trailing edge of the plume where the gas is being displaced by the back-flow of water leading to the disconnection of the gas phase into bubbles and ganglia that will become eventually immobile. [21] [36]

4.4 Land Model

Most models for relative permeability that account for hysteresis are based on the Land trapping model. [39] In fact, in the context of petroleum engineering applications, residual trapping has been studied thoroughly mainly to determine the ultimate oil recovery, whether during primary production or during water flooding. The same methodology is adopted to determine the CO₂ residual trapped saturation, which will enable the determination of the residual CO₂ storage capacity of a storage formation. [40]

The Land model links the residually trapped saturation to the initial gas saturation, by the following empirical relation:

$$S_{CO_2,r} = \frac{S_{CO_2,i}}{1+C S_{CO_2,i}} ; \quad (12)$$

Where $S_{CO_2,i}$ is the gas saturation at flow reversal, $S_{CO_2,r}$ is the residually trapped CO₂ saturation after imbibition, and C is the Land trapping coefficient, which is by definition an empirical coefficient characterizing the trapping strength. [39]

Inspecting this relation, it can be seen that the trapped saturation due to imbibition increases as the initial gas saturation increases.

Land Coefficient is computed from the bounding drainage and imbibition relative permeability curves as follows:

$$C = \frac{1}{S_{CO_2,r \max}} - \frac{1}{S_{CO_2 \max}} \quad (13)$$

Where $S_{CO_2,r \max}$ is the maximum trapped gas saturation and $S_{CO_2 \max}$ is the maximum CO₂ saturation reached.

The Land coefficient can take on all values greater than zero, with C=0 meaning a residual trapping efficiency of 100% as all the CO₂ present before imbibition will be trapped, whereas C=∞ results in zero trapping efficiency as none of the initial CO₂ is trapped. This being said we can conclude that C is inversely proportional to the residual trapping efficiency. [41] [42]

The Land model also divides the gas present in the reservoir in a part that is mobile (free to move) and another part that was trapped that does not contribute to the flow. This is important for the computation of the relative permeability- saturation curves after imbibition. In order to perform this computation, the free gas saturation also known as connected gas saturation is needed, as it is the saturation that is actually mobile, and it can be obtained from

the following equation Eq.14:

$$S_{CO2f} = \frac{1}{2} \left\{ (S_{CO2} - S_{CO2r}) + \sqrt{(S_{CO2} - S_{CO2r})^2 + \frac{4}{C} (S_{CO2} - S_{CO2r})} \right\} \quad (14)$$

Where S_{CO2f} is the saturation of CO₂ free to move (connected CO₂ saturation), S_{CO2} is the current gas saturation, S_{CO2r} is the residual gas saturation and C is the Land coefficient. [39]

This approach relates the imbibition relative permeability to CO₂ $k_{r,CO2}^i (S_{CO2})$ at a given saturation S_{CO2} , to the drainage relative permeability evaluated at the connected CO₂ saturation noted S_{CO2c} with the following equivalence:

$$k_{r,CO2}^i (S_{CO2}) = k_{r,CO2}^d (S_{CO2f}) \quad (15)$$

[41] [21]

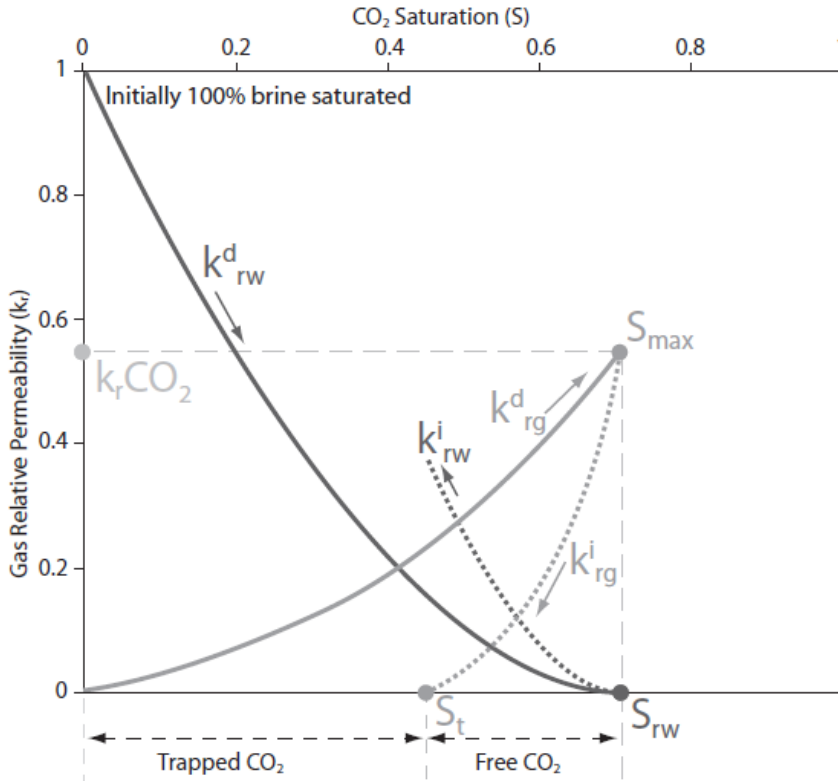


Figure 9:Diagram showcasing a typical CO₂ -brine relative permeability curves under the effect of hysteresis as well highlighting the distribution of CO₂ between a free CO₂ and trapped CO₂ after a first imbibition [43]

4.5 Snap-off

One of the main processes in which CO_2 is trapped as disconnected bubbles and ganglia after imbibition is known under the name of snap-off. So it's worthwhile to dig deeper into this phenomenon.

Since CO_2 is considered the non-wetting phase, thus once injected into the porous media it will invade the larger pores, leaving the brine in the tighter and smaller pores that are not yet invaded as well in the corners and crevices of the invaded pores. At the tail of the plume, an imbibition process takes place as the water displaces the CO_2 Fig.11. [37] During the imbibition process, the wetting film swells until the non-wetting phase loses contact with the solid. Subsequently, the center of the pore gets rapidly filled with water as this situation is considered unstable Fig.10. This phenomenon occurs first in the narrowest throat of the smallest pores and propagates progressively to larger ones. [44] [37]

The favorable conditions in which important snap-off occurs are mainly related to the formation wettability, pore geometry and connectivity, and the intensity of the brine's natural flow. It is worth mentioning that the snap-off phenomena can only be important if the formation is water-wet. This is due to the fact that the more the formation is water wet, the easier it is for the wetting layer to flow, which leads to more snap-off and CO_2 trapping. [37] The latter is reduced in the case of a mixed wet formation and is absent if the system becomes CO_2 -wet. The aquifers studied for storage are most likely to be water wet, however, due to some chemical reactions such as dissolution, the medium can be transformed into neutral and even CO_2 -wet medium. [45] [44] In addition, the larger the pores and the narrower the throats, the more likely to observe snap-off. On the other hand, a porous media with good pores connectivity, meaning that a single pore is connected to several throats, hinders the residual trapping. Equally important, a low brine imbibition flow rate favors the snap-off mechanism and results in higher trapping, since time is needed for the wetting layers to swell before the frontal advance of the wetting phase fills the pore space. [44]

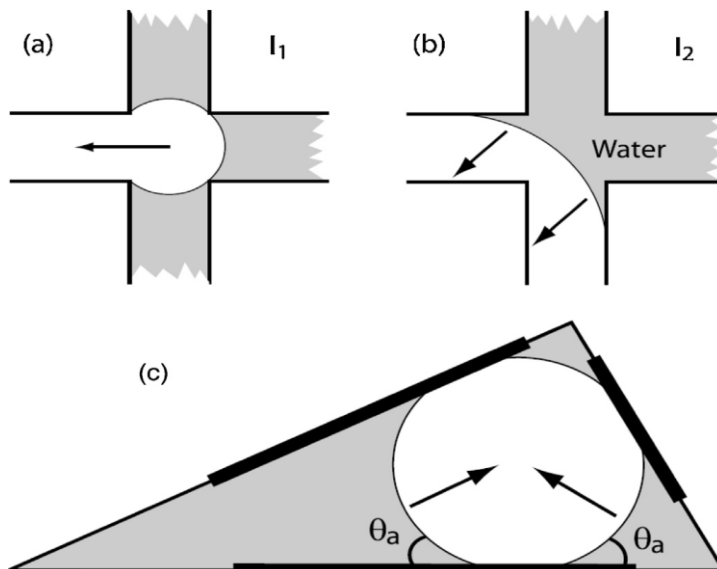


Figure 10: Scheme showcasing the snap-off phenomenon leading to entrapment of the CO_2 as non-connected bubbles. [44]

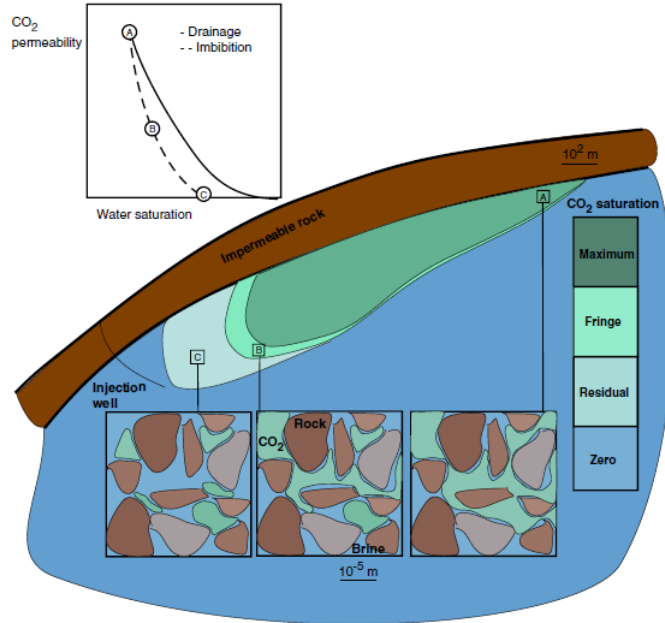


Figure 11: Sketch representing the state of the CO₂ plume after injection while focusing on highlighting capillary trapping at the trail of the plume. [44]

4.6 Capillary Pinning

In addition to the snap-off mechanism, an equally important phenomenon to capillary trap the CO₂ in heterogeneous reservoir is the capillary pinning. Capillary pinning is the result of the difference in capillary pressure between a layer of Coarse grained (CG) and Fine grained (FG) rocks. [46] This capillary pressure contrast between the two types of rocks results in CO₂ pinning in the CG rocks. The buoyant ascension of the CO₂ plume through interstratified rock types with different capillary pressure barriers will lead to CO₂ pinning within CG rocks due to the capillary contrast between CG and FG rocks. [47] Unlike the snap-off mechanism that only works during the imbibition process, capillary pinning occurs in drainage as well as in the imbibition phase. In addition, capillary pinning works at the scale of the heterogeneity, whereas snap-off only occurs at the pore scale, as mentioned earlier. Capillary pinning is strongly affected by the contrast in capillary pressure between the two types of rocks, and it increases with an increase in this contrast. As well, capillary pinning is more pronounced during gravity flow, far from the well, compared to viscous flow, in the vicinity of the well. [46]

4.7 Data Available in Literature

There has been a recent strong interest in expanding the database of relative permeability data concerning CO₂-brine system in the purpose of underground storage. In this part, all the relative permeability data published in literature thus far to my knowledge will be presented.

The different formations for which relative permeability data are available will be summarized in table 2.

Table 2: Relative permeability data present in literature.

Reference	Formation	k(mD)	$k_{rCO_2}(S_{wi})$	S_{wi}	Corey exponent Brine	Corey exponent CO ₂	Trapped Gas Saturation	Trapping efficiency
[48]	VikingFm #3	1558.65	0.09	0.6	1.33	4.34	0.22	0.56
	ClearwaterFm	0.0164	0.49	0.34	1.24	1.6	0.14	0.22
	Ellerslie Fm #2	3812.36	0.57	0.38	1.18	4.79	0.42	0.68
	Rock Creek Fm	65.03	0.04	0.48	2.19	1.9	0.47	0.91
	HalfwayFm	54.23	0.27	0.46	3.12	3.48	0.46	0.86
	BelloyFm	536.6	0.07	0.65	1.67	5.22	0.28	0.81
	GraminiaFm	133.9	0.14	0.44	1.42	4.98	0.38	0.68
	GilwoodFm	0.749	0.54	0.56	1.75	3.73	0.356	0.82
	Basal Cambrian Ss#2	0.0057	0.21	0.57	1.45	3.89	0.23	0.54
	Basal Cambrian Ss #3	252.5	0.15	0.49	1.63	1.35	0.4	0.79
	Basal CambrianSs #4	157.8	0.21	0.65	4.54	3.74	0.27	0.77
	BasalCambrianSs#5	0.03	0.32	0.27	1.21	5.48	0.52	0.71
	DeadwoodFm#1	103.66	0.10	0.48	1.8	7	0.38	0.75
	DeadwoodFm#2	69.11	0.09	0.59	1.5	4	0.29	0.71
	DeadwoodFm#3	137.9	0.25	0.65	1.2	6.57	0.24	0.69
Granite Wash	70.13	0.4	0.57	1.15	1.81	0.22	0.53	
[49]	Cardium#1	0.56	0.52	0.19	1.3	1.7	0.1	0.12
	Cardium#2	21.17	0.13	0.42	1.2	1.3	0.25	0.44
	Viking#1	2.7	0.33	0.55	2.9	3.2	-	-
	Viking#2	21.72	0.26	0.42	1.7	2.8	0.29	0.51
	Ellerslie	0.376	0.11	0.66	2.1	2.2	-	-
	Basal Cambrian Fm	0.081	0.54	0.29	1.8	5	-	-
[22]	Heletz	104	0.93	0.22	7.34	2	0.2	-
	Inmar	425	0.75	0.65	7	2	-	-
	Arqov	13	0.31	0.11	4.17	2	-	-
[50]	In Salah	2.5-7	1	0.3	-	-	-	-
[51]	Ketzin	20-70	0.87	0.57	-	-	-	-
[52]	Frio formation	56.57	0.7	0.18	-	-	-	-
[53] [54]	Ustira(Sleipner)	1000-8000	0.75	0.11	-	-	0.24	-
[20]	Berea Sandstone	430	0.06	0.62	-	-	-	-
	Otway	45	0.6	0.44	-	-	-	-
[55]	Cranfield		0.6	0.3	2	4	-	-
[41]	Mt Simon	7.5	0.46	0.22	9	2	0.21	0.26
	Paaratte	1156	0.3	0.05	8	2	0.33	0.34
	Tuscaloosa	220	-	0.05	17	2	0.31	0.32
	Berea Sandstone	914	0.38	0.11	6	2	0.31	0.34
[42] [56]	Captain	700-1500	0.6	0.12	-	-	-	-

[57]	Bentheimer	-	0.8	0.08	4.4	4.6	-	-
[58]	Berea Sandstone	308	0.92	0.33	3.84	3.84	-	-
[59]	Boise Sandstone	1866	-	0.2	-	-	0.32	0.4
[60] [61]	Tako Sandstone	55.4	-	0.15	-	2	0.28	-
	Captain#1	2048	0.96	0.33	-	-	0.38	0.56
	Captain#2	1025	0.92	0.3	-	-	0.29	0.41

By inspecting table 2, it can be seen that the data provided by the experiments done, especially those performed by [49] [48], resulted in relatively high S_{wi} and low endpoint relative permeability to CO_2 . Therefore, it is in our interest to learn more about the techniques used in these experiments in order to better understand the data and the reasons behind the results. It is then worthwhile to dig a bit deeper in the different techniques applied to measure the relative permeability relations.

4.7.1 Steady State Tests

One way to measure relative permeability is through the steady-state test, which is based on achieving a steady-state saturation along the full length of the core and measuring the relative permeability to one or both phases while keeping the saturation constant. [62] [21] The test consists in co-injecting CO_2 and brine in different proportions (fractional flow rate). The fractional flow rate of CO_2 f_{CO_2} can be expressed as the ratio of CO_2 flow rate $F_{CO_2}^{Tres,Pres}$ and the total brine plus CO_2 flow rate $F_{CO_2}^{Tres,Pres} + F_{H_2O}^{Tres,Pres}$:

$$f_{CO_2} = \frac{F_{CO_2}^{Tres,Pres}}{F_{CO_2}^{Tres,Pres} + F_{H_2O}^{Tres,Pres}} \quad (16)$$

The main condition of a steady-state experiment is that steady-state equilibrium should be reached across the core for every fractional flow, and only then the data can be collected and the calculation can be done. [63] [64] This procedure is repeated for all fractional flow rates till reaching 100% CO_2 -flooding. [63]

In the case of a homogenous sample (same k_r - S relation throughout the core) and a constant saturation of each phase throughout the core, then based on Eq.10, the pressure gradient in the core will be constant. As well, the capillary pressure will be constant across the core, meaning that the pressure gradient will be equal for each phase, $\frac{dP_i}{dx} = \frac{dP}{dx}$, enabling the simplification of Eq.10 into:

$$q_i = - \frac{A k_{r,i}(S_i)}{\mu_i} \frac{\Delta P}{L} \quad (17)$$

Thus, the relative permeability can be obtained by measuring the pressure drop across the core while circulating CO_2 and/or water through the core, and by monitoring the saturation with an x-ray CT scanner. [21]

Steady-state methods provide the most accurate measurement of relative permeability,

however, their only disadvantage is that the equipment is complex and the method is time-consuming. [65]

Several techniques exist to perform the steady-state experiments such as the Penn State method, the single sample dynamic method, and the Hassler method. [66] The two most common are the Penn State and the single sample dynamic method, and they both require a constant total volumetric flow rate. The difference between the two methods is in the way they deal with the capillary end effect (see section 4.7.3 below). The single sample dynamic method uses a very high rate so that the effect is limited to a small region at the boundary of the core. While on the other hand, the pressure measurement in the Penn method is performed in the central part of the core, far from the boundaries where the capillary end effect is more pronounced. [21] [67]

Meanwhile, the Hassler method requires keeping the capillary pressure between the two fluids constant by maintaining an equal pressure gradient in both phases. Nevertheless, the application of this method has been limited due to the complex challenges faced during its implementation. [62] [67]

4.7.2 Unsteady Methods

The unsteady methods consist of both core flooding and centrifugal experiments. In the former, the core is initially saturated with the phase to be displaced and then the core is flooded with a single phase. [68] The initial condition of the core could be at 100% saturation of the phase to be displaced or at irreducible saturation of the displacing fluid and that choice depends on the application. [21] It is worth noting that the time required to perform the relative permeability measurements using the unsteady state methods is significantly less compared to the steady-state method. [62] [68]

In a core flooding experiment, the injection can be either performed at a constant rate or at a constant pressure while continuously measuring the differential pressure across the core and keeping track of the injected volume. [62] [21] [69]

The production data are analyzed and then a set of relative permeability can be obtained by the application of several mathematical methods. [69] The most commonly used mathematical methods include the Welge, Johnson-Bossier-Namnam (JBN), and Jones-Rozelle. [69] The applicability of these methods is constrained by the assumption of the Buckley-Leverett equation; an incompressible and immiscible flow, a perfectly dispersed flow, and a negligible gravity and capillary effects. [21] The latter problem can be circumvented by the application of very high rates. Nonetheless, this can be accompanied by other problems such as fines mobilization and viscous instability. As well, performing this experiment under an unfavorable viscosity ratio like in the case of CO₂-brine will lead to poor sweep efficiency, which will eventually lead to longer experiment time and thus contradicting the common perception that unsteady state techniques are quicker than steady-state methods. [21]

The unsteady methods are further sub-divided into four categories: high rate, low rate, centrifuge, and stationary liquid method. [62]

The high rate method is the most widely adopted unsteady method. The reason behind the high rate of the injected fluid is to minimize the end effect. Both the saturation and the pressure drop are continuously monitored throughout the experiment. [62] [70] Meanwhile,

in the low rate techniques the capillary effects are more pronounced and that is thought to better replicate in-situ flow velocities. In order to decouple the effect of the capillary effect on the relative permeability, data processing and numerical modeling have been developed. By implementing these data processing techniques, the capillary pressure and relative permeability relationships can be obtained simultaneously. [62]

The centrifuge method is yet another technique able to measure the relative permeability and capillary pressure simultaneously. The rock sample is mounted on a rotator cup rotating at a constant speed, which drains the fluid at an exponentially decreasing rate. The capillary pressure relationship can be determined by measuring the rate of fluid drainage. Nonetheless, in order to obtain the relative permeability relations, similar data techniques from the low rate method are applied. [62] [70]

Regarding the stationary liquid method, the relative permeability to gas can be measured with pressure or pulse decay. In this method, the liquid saturation remains constant while the gas rate is varied with time. [62]

4.7.3 Main Problems with Relative Permeability Measurements

The issue of having high irreducible water saturation and low relative permeability endpoint to CO₂ was raised by [21] and [23], and suggested two main reasons behind the discrepancy of the results shown in the table 2.

First, the capillary end effect is considered one of the main issues in core flooding tests. It is the result of capillary pressure discontinuities at the inlet and outlet faces of the core leading to capillary pressure and saturation gradient across the length of the core, which may complicate the relative permeability calculation. The capillary end effect seems to be more important downstream than upstream as it is leading to a higher wetting phase saturation at the outlet compared to the remainder of the core. [20] [23] [21] [64] This will result in a problem for the unsteady methods that rely on outlet measurements without taking the capillary forces into account. The measurements using steady-state techniques are equally affected. The saturation gradient present will produce a difference between the pressure drop across the core that causes the wetting phase to flow and the pressure drop that causes the non-wetting phase to flow. The latter is actually higher than the former, and the difference between the two is equal to the capillary pressure difference between the two ends of the core. This will cause an underestimation of the relative permeability to the non-wetting phase as it is assumed that the pressure drop in the wetting phase is equal to the one in the non-wetting phase. [21]

This problem could be dealt with in one of two distinct ways, to eliminate the end effect or to take it into account by applying an adequate mathematical model.

To eliminate the end effect, myriad technical solutions have been proposed, either by enabling direct control on the capillary pressure (Hassler method) or by performing the measurement far enough from the two ends of the sample (Penn State method). [21] [29] In addition, the problem can be circumvented by an increase in the injection rate (single dynamic method) due to the fact that as the injection rate increases, the length over which the boundary saturation gradient is observed decreases. [23] [62] [64]

On the other hand, the application of mathematical models consists in explicitly accounting

for the capillary effect by imposing an adequate boundary condition. However, the success of this method is hindered by the lack of understanding of the actual boundary condition during a core-flood experiment. One way to implement the mathematical model is to impose a zero capillary pressure value. As a consequence, both the saturation and the relative permeability to the non-wetting phase will be set to zero. An alternative way is to consider a non-zero value. Some propose that the capillary pressure at the outlet should be equal to the entry capillary pressure [67] (minimum pressure at which the relative permeability to the non-wetting phase is non-zero), while others will allow the outlet saturation to vary according to Darcy's law. [21]

Secondly, the capillary pressure limitation is another issue that can lead to obtaining low-endpoint values during both steady and unsteady experiments and it is mainly attributed to having an unfavorable viscosity ratio. [58] This is in fact relevant in the case of scCO₂/brine as the low viscosity of the injected gas limits the attainable level of capillary pressure during the core-flood. The outlet end effect has a direct effect on unsteady methods that are based on effluent data, as it precludes reaching high non-wetting phase saturation. Meanwhile, it is very difficult to meet the basic condition required during a conventional steady-state experiment, given that the endpoint is approached and that allows the application of the integral form of the extended Darcy's law in one dimension. The endpoint by definition, is reaching the part of the capillary curve where pressure varies steeply with saturation. In addition, it is required in a co-injection scheme to have a constant saturation and capillary pressure across the core, which is not the case for the capillary pressure as it is very difficult to achieve this condition without any control on the capillary pressure itself. Therefore, the decreasing capillary pressure in the core is leading to an underestimation of the relative permeability to the non-wetting phase [58] [21]

In addition, it was found by [58], that by changing the experiment's technique, they were able to reach a high relative permeability endpoint to the non-wetting phase, which confirms that the low endpoint of the relative permeability and the high irreducible saturation are indeed an artefact of the techniques previously implemented to make relative permeability measurements.

5 Model and Simulation

In this section the aquifer model will be described and the simulations conditions and the different parameters used will be presented. The aquifer parameters are generic and are not taken from a specific field or case study but they were set to build a model on which the sensitivity analysis can be performed.

5.1 Aquifer Model

The simulation tool utilized in this work is GEM Compositional and Unconventional Simulator from Computer Modelling Group (CMG). The 3D model was created to simulate an aquifer with the following characteristics:

The aquifer was set at a depth of 1500 m (top layer). The initial pressure was set at 150 bar and the aquifer was considered to be at a temperature of 50°C. A Carter-Tracy infinite aquifer with the leaking option enabled was included in order to simulate an aquifer with a flowing boundary.

The aquifer has a size of $60.76 \cdot 10^6 \text{ m}^3$ Fig.12, the formation is a homogeneous and isotropic sandstone having a porosity of 0.2 and a permeability of 200 mD.

The grid was designed with a grid refinement configuration near the wellbore to better simulate near wellbore phenomena. The model consists of a total of 8748 cells ($27 \times 27 \times 12$) divided equally in the i and j direction and 12 levels (k direction). All layers in the vertical direction were set to have a thickness of 2 m except for the second layer which is the cap rock with a thickness of 10 m and a permeability of 10^{-7} mD. As well, the first layer has a thickness of 1m but its permeability is the same as the one of the aquifer.

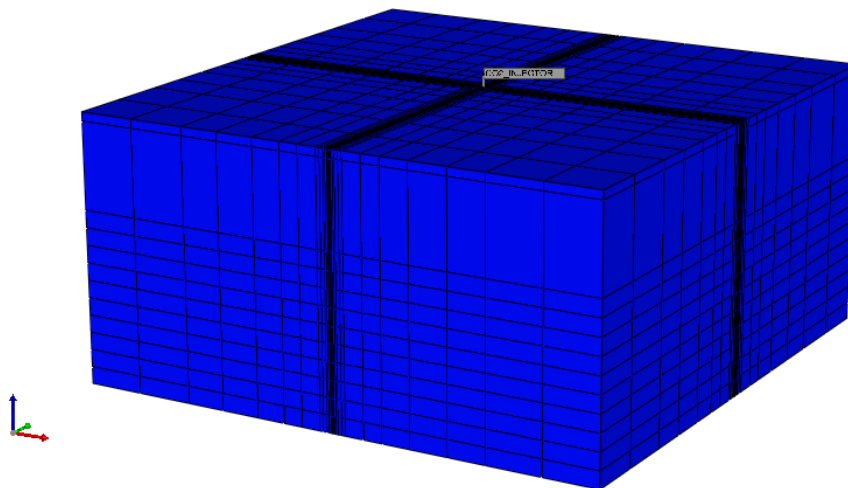


Figure 12: 3D representation of the aquifer model

The CO₂ injector well was placed at the center of our aquifer having the following coordination (14,14) in the (i,j) plane and the perforation were performed in the lower part

of the formation raging from the layer 9 to layer 11. The choice of the interval of perforation was backed by the fact that it is preferable to maximize the length of the CO₂ path from the well to the cap rock. [71] [72] The CO₂ was injected according to a ramp-up injection strategy in order to avoid pressure peaks, with injection rates equal to 50,000 scm³/day for the first three months, then 100,000 scm³/day for one month, and then 200,000scm³/day for 3 months as seen in the picture (Fig.13). The monitoring period after the injection was 200 years.

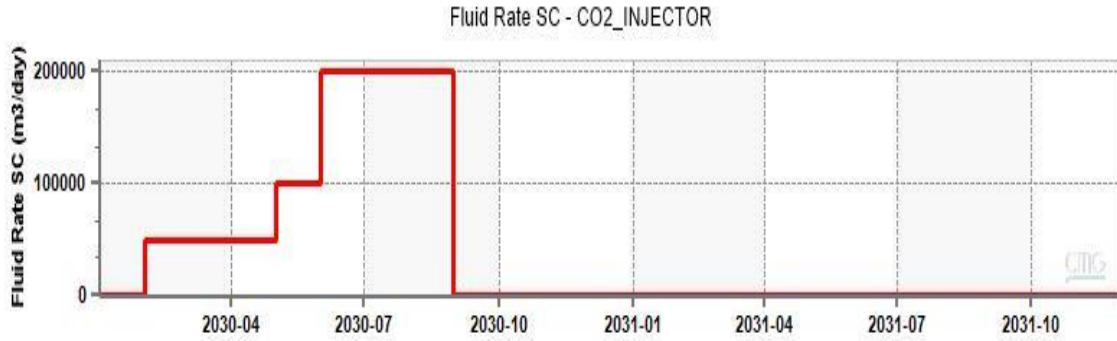


Figure 13:CO₂ injection history

To be able to study the dissolution trapping mechanism, CO₂ solubility with the formation water was enabled by activating the Henry solubility option for the CO₂ component. The Henry constant for CO₂ implemented in the software is dependent on pressure, temperature and salinity.

The salinity of the brine was 300,000 mg L⁻¹, the pH was set to 5.5 and the composition of the water was as following:

Table 3:Composition of the brine water

Component	Concentration in ppm
Ca ²⁺	36900
Mg ²⁺	3700
K ⁺	5640
Na ⁺	65300
SiO ₂	181
Cl ⁻	176100

5.1.1 Geochemical Model

In this study the interaction of CO₂ with the formation water and rock were considered. In order to assess that, the different equations already mentioned in the previous parts have been included.

The aqueous reactions mentioned in Eq.1 were added:

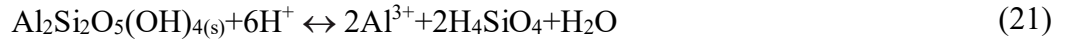


As well, the water dissociation equation was included:



In addition, since the rock is a sandstone, the mineralization reactions of CO_2 with the following minerals were included: calcite, quartz, kalonite, illite and albite, as discussed in the mineral trapping part (3.5).

Reactions included are as follows:



5.1.2 Relative Permeability and Capillary Pressure

As previously reported in the literature, the Bentheimer formation is provided with correlations for both relative permeability curves (wetting and non-wetting phase) as well as for capillary pressure curves (drainage and imbibition). For this reason, it was adopted as the base case simulation.

The drainage relative permeability curves were based on the power law for both the wetting and the non-wetting phase:

$$k_{\text{rnw}} = k_{\text{rnw}}(\text{S}_{\text{wi}}) (1 - \text{S}_{\text{w}}^*)^n \quad (24)$$

$$k_{\text{rw}} = (\text{S}_{\text{w}}^*)^m \quad (25)$$

With S_{w}^* as the effective saturation expressed as $\text{S}_{\text{w}}^* = \frac{\text{S}_{\text{w}} - \text{S}_{\text{wi}}}{1 - \text{S}_{\text{wi}}}$; $k_{\text{rnw}}(\text{S}_{\text{wi}})$ is the non-wetting relative permeability at the irreducible water saturation and n and m are the power law coefficient to the non-wetting and wetting phase respectively. [29] [57]

To compute the drainage capillary pressure, the power law as presented by Brooks-Corey was also adopted [33]:

$$P_{\text{c}}^{\text{d}} = P_{\text{e}} (\text{S}_{\text{w}}^*)^{-1/\lambda} \quad (26)$$

With P_{e} as the capillary entry pressure set at 3.7 kPa; λ is the pore size distribution factor and it was set to 2.7 [57].

The imbibition capillary curve was computed in a similar way to the drainage curve but with some modification as following:

$$P_c^i = P_{ci} ((1 - S_{nw,f}^*)^{-1/\lambda} - 1) + P_s \quad (27)$$

Where P_s is the snap-off pressure given as 1.165 kPa , $S_{nw,f}^*$ is the effective mobile non-wetting phase saturation that can be calculated from the Eq.14 and P_{ci} is found by equating the drainage and the imbibition capillary pressure curve at irreducible water saturation. [57]

5.2 Sensitivity Analysis

In order to investigate the effects of the relative permeability curves on the final storage of CO₂ in a saline aquifer it was decided to perform a sensitivity analysis by varying all the parameters that alter the relative permeability curves as well as the capillary pressure curves. In each simulation only one parameter was varied from the base case value in order to isolate and interpret its effect on the final CO₂ stored in the formation. The different parameters and their corresponding values have been summarized in the table 4 where the cell highlighted in green is the parameter that was varied in the corresponding simulation (Sim). All the simulations were performed under the same injection strategy and for the same monitoring period mentioned before. Therefore, the same amount of CO₂ was injected for the same duration in all simulations.

Table 4: Different values adopted to perform the sensitivity analysis.

	Base Case	Sim1	Sim2	Sim3	Sim4	Sim5	Sim6	Sim7	Sim8	Sim9	Sim10	Sim11	Sim12	Sim13	Sim14	Sim15
S_{wi}	0.2	0.08	0.35	0.66	0.2	0.2	0.2	0.2	0.2	0.2	0.2	0.2	0.2	0.2	0.2	0.2
$k_{rCO_2}(S_{wi})$	0.8	0.8	0.8	0.8	0.5	0.1	0.8	0.8	0.8	0.8	0.8	0.8	0.8	0.8	0.8	0.8
Land Coefficient C	1.25	1.25	1.25	1.25	1.25	1.25	0.17	3.00	8.00	1.25	1.25	1.25	1.25	1.25	1.25	1.25
P_e	3.7	3.7	3.7	3.7	3.7	3.7	3.7	3.7	3.7	0	(no P_c^D)	8.27	3.7	3.7	3.7	3.7
Corey exponent for brine	4.4	4.4	4.4	4.4	4.4	4.4	4.4	4.4	4.4	4.4	4.4	4.4	2.2	9	4.4	4.4
Corey exponent for CO_2	4.6	4.6	4.6	4.6	4.6	4.6	4.6	4.6	4.6	4.6	4.6	4.6	4.6	4.6	2.3	7

As mentioned earlier, the parameters used in the base case were taken from the experiments on the Bentheimer Sandstone [57], however since the Bentheimer formation had the lowest irreducible water saturation found in the literature ($S_{wi}=0.08$), a more common value ($S_{wi}=0.2$) was adopted for the base case. Furthermore, since $S_{CO_2,r}$ was the parameter imposed to control Land model in GEM software, the Land coefficient was chosen equal to 1.25 for the base case instead of 1.75 as mentioned in [57], as this will lead to having a $S_{CO_2,r}$ of 0.4 using Eq.12.

First, the target was to investigate the effect of the irreducible water saturation S_{wi} . Based on the summarized parameters in table 2 it was possible to identify that the low boundary of S_{wi} is 0.08 belonging to the Bentheimer formation [57] whereas the high boundary of S_{wi} is 0.66 for the Ellerslie formation in Canada [49]. In addition to the above-mentioned values, an intermediate value $S_{wi} = 0.4$ was selected. Similarly, the lowest value for endpoint of the relative permeability to CO_2 ($k_{rCO_2}(S_{wi})$) was 0.1 and 0.8 was taken as the high boundary. An intermediate value of 0.5 was also chosen. For the Land coefficient a low boundary of 0.17 (high trapping) belonging to the Canadian formation Halfway [48] was identified. Whereas, the highest value is for the Cardium 2 formation [48] with a Land coefficient of 8 (very low trapping); and an intermediate value of 3 was taken within this range.

Then the effect of the capillary pressure was investigated. Initially, a case in which capillary pressure was opted out from the model was simulated. Then, to study the effect of hysteresis a simulation was performed without including the imbibition capillary pressure curve. Furthermore, the value 8.27 kPa was taken as an upper boundary to the entry capillary pressure as it corresponds to a capillary fringe of 10 m.

To inspect the effect of the shape of the relative permeability curves, the Corey exponents were varied. As a lower boundary, the half of Corey parameters adopted in the base case were taken. For the upper boundary, $n=7$ was adopted as the maximum exponent for gas, while the maximum exponent for water was taken as $m=9$, based on the values present in the literature. The $m=17$ of the Tuscaloosa Sandstone was opted out due to the fact that it is an extremely heterogeneous rock, as it is a poorly sorted conglomerate. [41]

6 Results and Discussions

In this section the results of all the simulations summarized in table 4 are presented and discussed to be able to identify the effects of all the parameters that interplay in the relative permeability and capillary pressure curves. In each part the results obtained by varying only one parameter while all the other parameters stay equal to their base case values are presented.

6.1 Effect of Irreducible Water Saturation

Three simulations were performed by varying the S_{wi} from 0.08 as the lower boundary to 0.66 as the higher boundary, while passing by an intermediate value of 0.4. The relative permeability to CO_2 curves for different S_{wi} are represented in Fig.14, and the results of the different simulations performed are summarized in table 5.

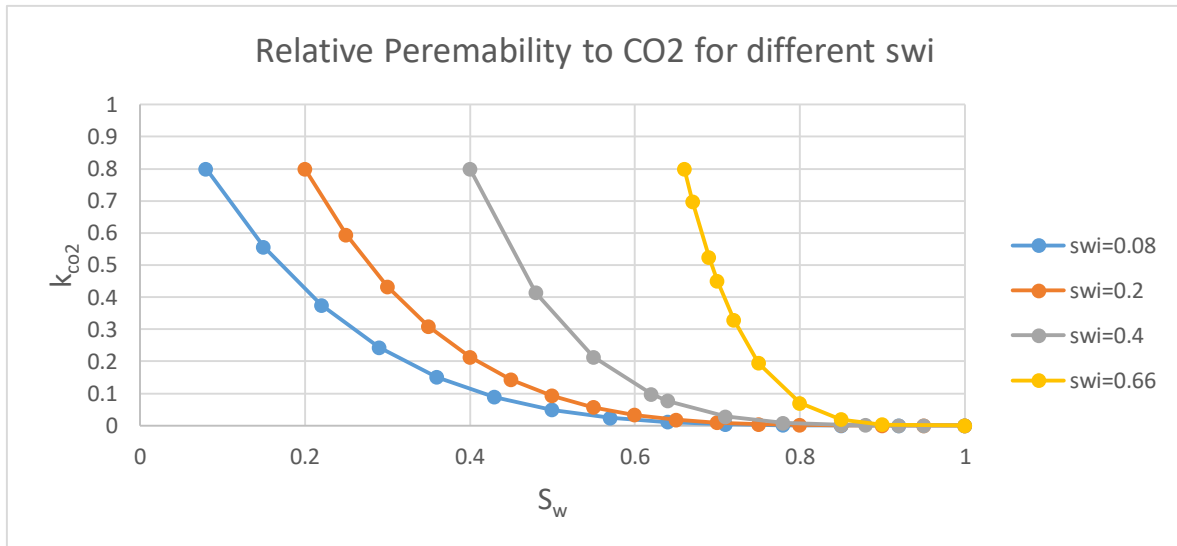


Figure 14:Relative permeability to CO_2 for different S_{wi}

Table 5: Distribution of CO_2 among the different trapping mechanism by varying irreducible water saturation.

Trapping mechanism	Sim1 ($S_{wi}=0.08$)	Base Case($S_{wi}=0.2$)	Sim 2 ($S_{wi}=0.4$)	Sim 3 ($S_{wi}=0.66$)
	Percentage			
Residual	50.32%	51.94%	52.24%	61.90%
Solubility	13.24%	14.00%	15.71%	22.46%
Ionic	0.03%	0.03%	0.03%	0.04%
Mineral	1.45%	1.50%	1.66%	2.27%
Structural/ Hydrodynamic	34.96%	32.53%	30.36%	13.34%

By inspecting the variation of the residually trapped CO₂, it can be observed that as the irreducible water saturation increases the amount trapped residually increases. This can be attributed to the fact that as the irreducible water saturation increases the pore space available for the CO₂ plume decreases, which will push the plume to expand and invade more pores (see Fig. 16,17 & 18). As mentioned before, the snap-off mechanism mainly occurs at the tail of the migrating plume, thus the more the plume migrates, the more important is the residual trapping mechanism. The observed results are in fact aligned with the results found by [46], as they mentioned a decrease in the snap-off with a decrease with the irreducible water saturation.

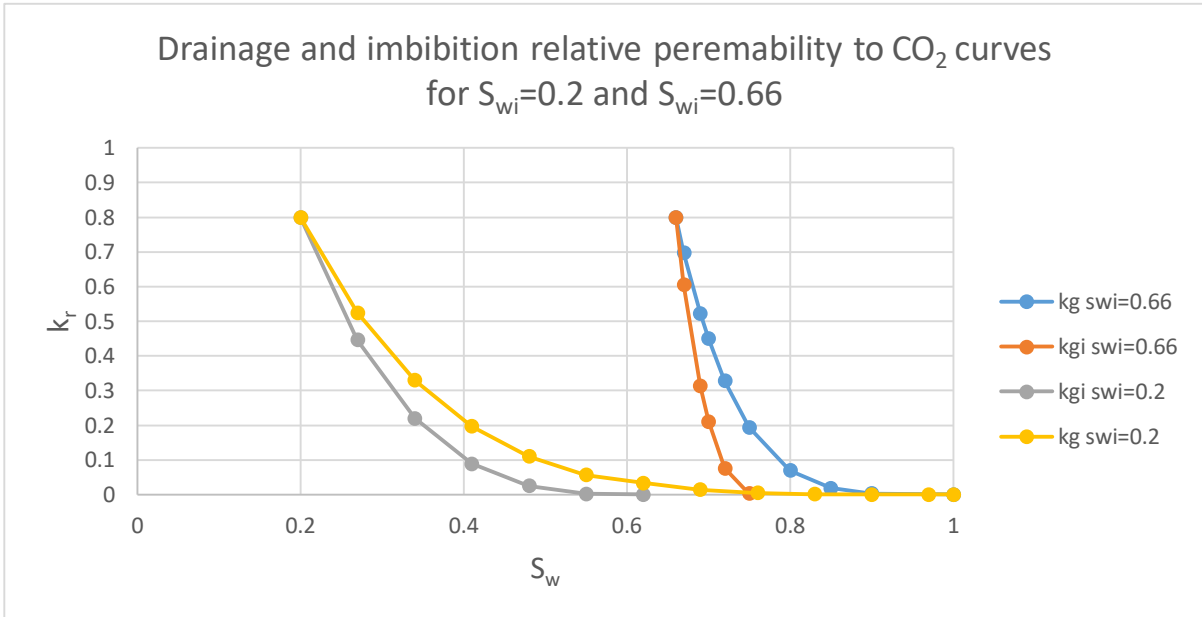


Figure 15: Plot of the drainage and imbibition curves of CO₂ for Swi of 0.2 and 0.66

Another aspect impacting on the increase in the residual trapping of CO₂ is that the imbibition curve is steeper and the range of saturation where CO₂ can be present as a free phase (mobile) is smaller in the case of high irreducible water saturation. This can be clearly seen in the plot of Fig. 15.

Considering now the dissolved share of the CO₂, it can be seen in table 5 that the dissolved portion of the injected CO₂ increases with an increase in the irreducible water saturation.

This increment can be studied at pore level and at field level. At pore level, the increase of the irreducible water saturation leads to an increase in the volume of water that remains inside the pore after the invasion of CO₂. This means that the CO₂ present in the pores will be in contact with higher volumes of water as the irreducible water saturation increases. This will be translated into an increase in the concentration gradient between the two phases, which will enhance the mass transfer mechanism.

At field level, as the irreducible water saturation increases, the CO₂ plume will tend to expand more and reaches more pores, which can be seen in Fig. 16, and 17. This will increase the area of contact between the CO₂ and the formation brine, and as a consequence more CO₂ is dissolved in the brine. The results concerning dissolution of CO₂ while varying the

irreducible water saturation are aligned with the results found by [73], as they found that the increase of irreducible water saturation increases the dissolution trapping.

Concerning the mineral trapping, it can be seen that as the irreducible water saturation increases the mineral trapping increases. This increase can be totally attributed to the increase in CO₂ dissolution, because as mentioned in the mineral trapping part (3.5), the dissolution is considered a precursor to the mineralization as the mineralization reactions requires that the CO₂ is dissolved in the brine so that it releases the carbonic acid that can eventually participate in the mineralization reactions. Nonetheless, no change in the ionic trapping was witnessed in all the simulations varying the irreducible water saturation and it remained constant at really low levels of almost 0.03% of the total trapped CO₂.

Regarding the structurally trapped CO₂, we can observe a decreasing trend as the irreducible water saturation increases, and that is due to the fact that the share of the trapping by other mechanisms is increasing at the expense of the structural trapping mechanism.

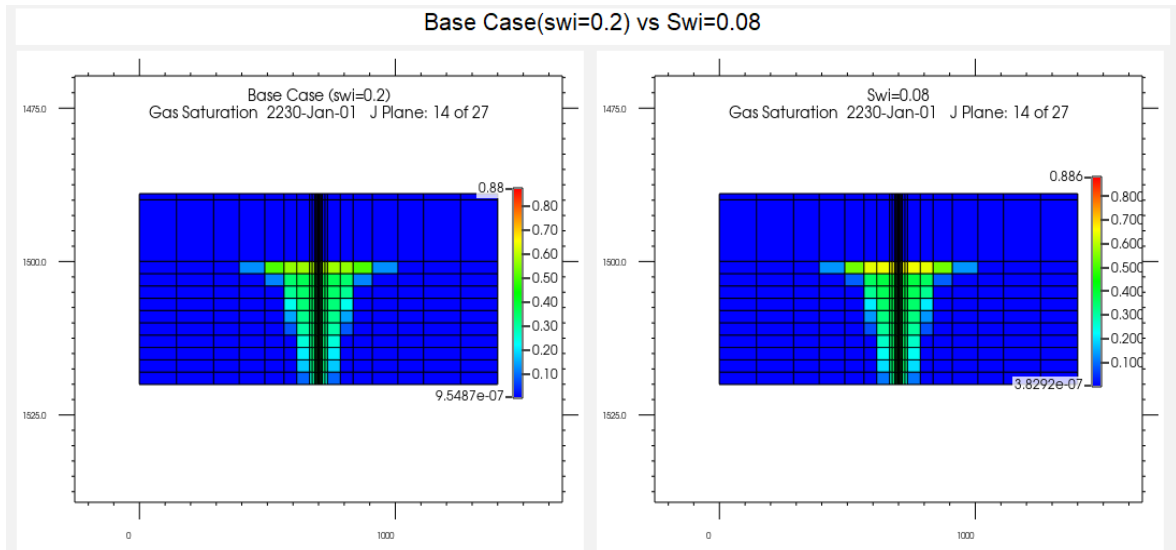


Figure 16: The distribution of the gas saturation at the end of the simulation (200years) for the base case (left) and $S_{wi} = 0.08$ (right)

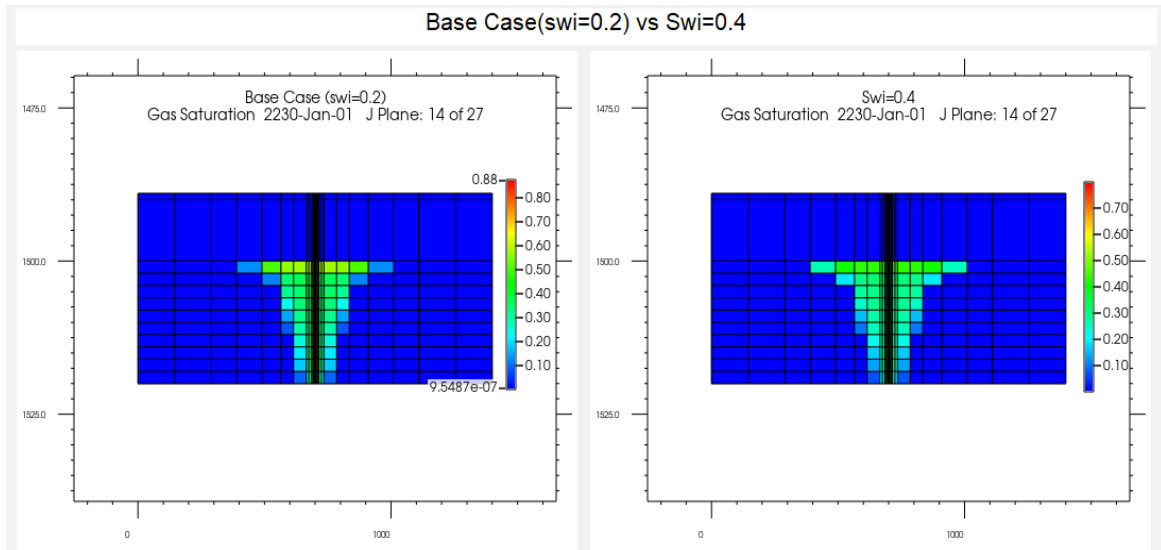


Figure 17: Distribution of gas saturation at the end of the simulation (200 years) for the base case (left) and $S_{wi} = 0.4$ (right)

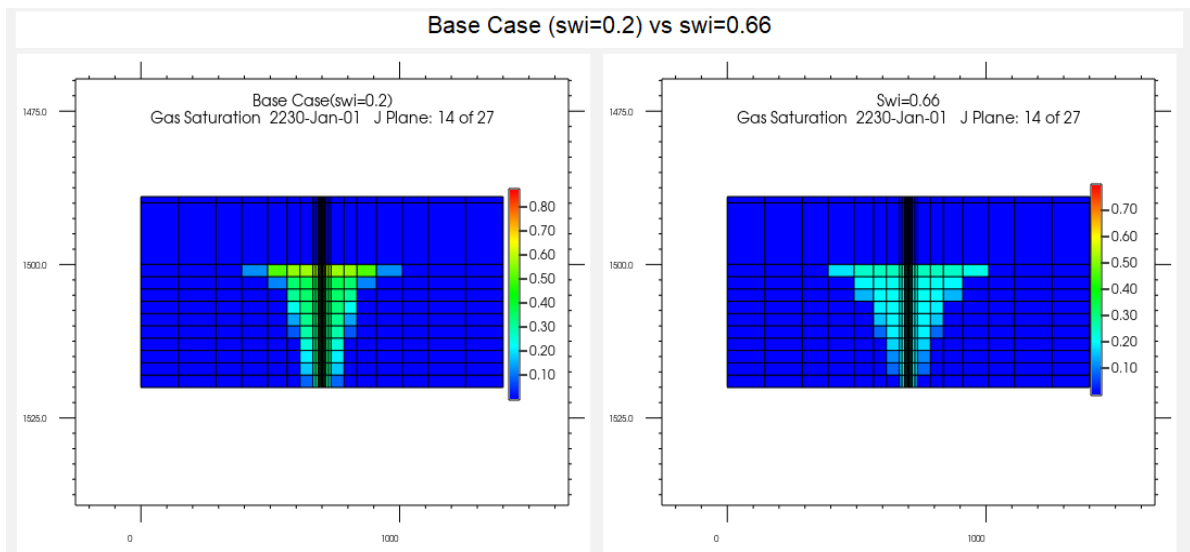


Figure 18: : Distribution of gas saturation at the end of the simulation (200 years) for the base case (left) and $S_{wi} = 0.66$ (right)

As mentioned earlier and as we can see from the Fig. (16,17&18), the plume extension is increasing with an increase of irreducible water saturation. This confirms that as the plume expands all three main trapping mechanisms (residual, dissolution and mineralization) become more important- but for different reasons.

6.2 Effect of the Endpoint of the Relative Permeability to CO₂

The values adopted for the endpoint of the relative permeability to CO₂ were 0.5 and 0.1 and are compared with the base case which has a value of 0.8. The $k_{rCO_2}(S_{wi})= 0.1$ is considered as an extremely low value knowing that the non-wetting fluid is CO₂, but for the sake of the sensitivity analyses this value was adopted in order to study the effects of the endpoint.

The relative permeability curves to CO₂ for the different endpoints are represented in the plot Fig.19, and the results for the simulations are summarized in the table 6.

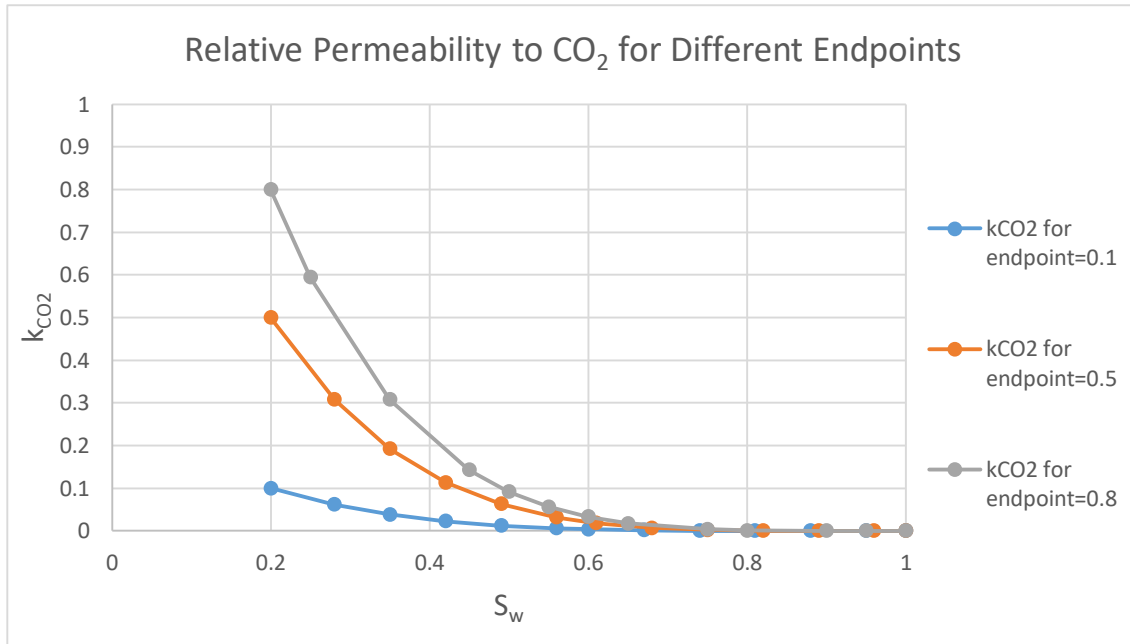


Figure 19:Relative permeability to CO₂ for the different endpoints

Table 6: Distribution of CO₂ among the different trapping mechanism for the different endpoint of the relative permeability to CO₂.

Trapping mechanism	Base case ($k_{rCO_2}(S_{wi})=0.8$)	Sim 4 ($k_{rCO_2}(S_{wi})=0.5$)	Sim 5 ($k_{rCO_2}(S_{wi})=0.1$)
	Percentage		
Residual	51.94%	54.04%	55.07%
Solubility	14.00%	14.85%	12.12%
Ionic	0.03%	0.03%	0.02%
Mineral	1.50%	1.55%	1.36%
Structural/ Hydrodynamic	32.53%	29.54%	31.42%

By investigating table 6, it can be seen that the lower the endpoint of the relative permeability to CO₂, the higher the portion trapped residually. One explanation for the increment is that by reducing the endpoint, the relative permeability curve is shifted downwards Fig.19. As a consequence, the CO₂ is more readily trapped by the brine during imbibition.

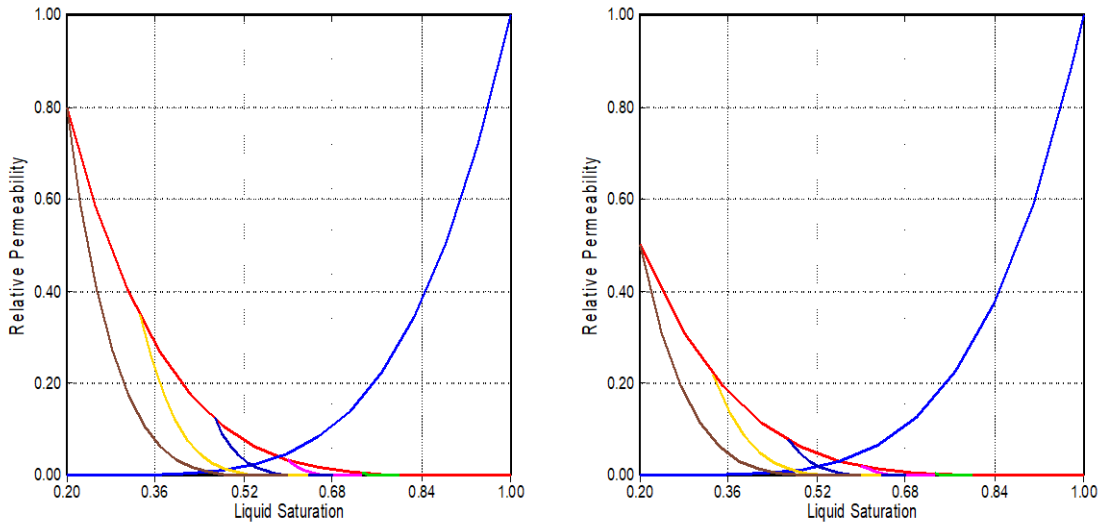


Figure 20: Imbibition curves and Land model for a $k_{rCO_2}(S_{wi})=0.5$ (right) and the base case with $k_{rCO_2}(S_{wi})=0.8$ (left).

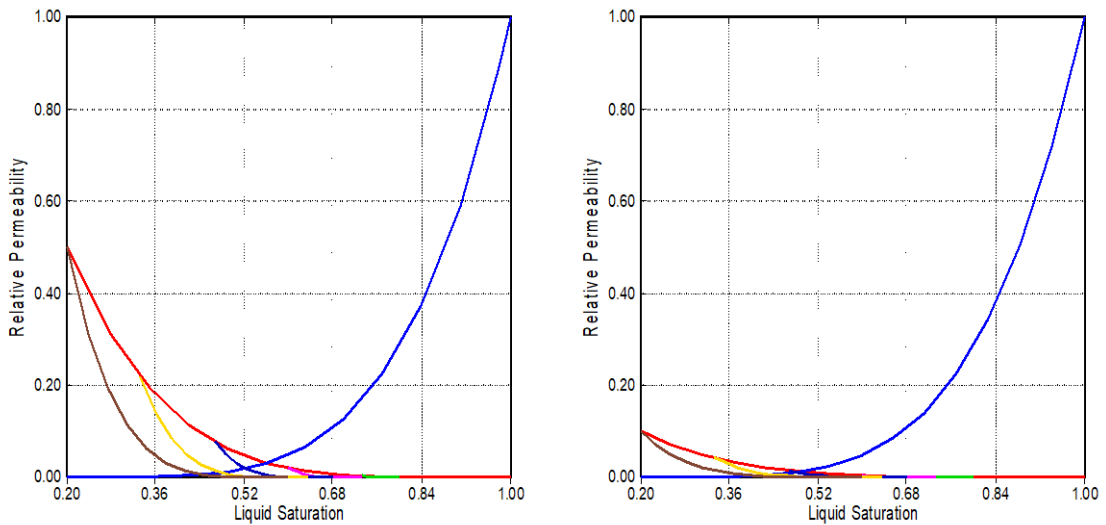


Figure 21: Imbibition curves and Land model for a $k_{rCO_2}(S_{wi})=0.1$ (right) and the base case with $k_{rCO_2}(S_{wi})=0.8$ (left).

The plots in Fig.20&21 show the imbibition curves of cases $k_{rCO_2}(S_{wi}) = 0.5$ and 0.1 respectively, compared to the base case. The plots can confirm what was presumed earlier,

as it can be seen that by lowering the endpoint of the relative permeability to CO₂, the corresponding imbibition curves reach very low permeability at a high gas saturation which leads to more gas being residually trapped, which explains the results listed in table 6.

Concerning the CO₂ dissolution, one might expect that the decrease of the relative permeability endpoint will lead to a decrease in the dissolved quantity of CO₂. That would be based on the fact that the lower permeability will limit the area of contact of the CO₂ plume with the formation brine, leading to lower dissolved quantity as we can see in Fig. 22 & 23. However, this is only true for the case where $k_{rCO_2}(S_{wi})=0.1$, because the case where $k_{rCO_2}(S_{wi})=0.5$ resulted in a higher percentage of dissolved CO₂ than the base case $k_{rCO_2}(S_{wi})=0.8$. In a way to explain this, the variation of the dissolved CO₂ in the brine in function of time for the base case and the case where $k_{rCO_2}(S_{wi})=0.5$ was inspected. It was seen that for the first 150 years the dissolved CO₂ is more or less equal in both cases, but after that, a gap between the two trends starts to build up Fig.24. As well, the variation of the residually trapped CO₂ in both cases was investigated and it was found that around the same time, the gap between the two cases starts to decrease Fig.25. In fact, in the year 2192 the difference between the quantity residually trapped in the case of $k_{rCO_2}(S_{wi})=0.5$ and base case is $0.25 \cdot 10^8$ mol, and this difference decreased to $0.23 \cdot 10^8$ mol at the end of the simulation. In parallel, the difference in quantity dissolved between the two cases at the same date was $0.07 \cdot 10^8$ mol and it increased to $0.09 \cdot 10^8$ mol at the end of the simulation. Performing the calculation of the difference of the gap between the year 2192 and 2230, it resulted in $\Delta_{trapped}=-0.02 \cdot 10^8$ mol while $\Delta_{dissolved}=+0.02 \cdot 10^8$ mol. Thus, the gap decrease by the residual trapped mechanism is in fact the same gap increase in the dissolved case. Therefore, the increase of the dissolved CO₂ while $k_{rCO_2}(S_{wi})$ is decreased can be explained by the fact that some of the residually trapped CO₂ at early times starts to dissolve, which can lead to an increase in the dissolved quantity. However, it can be seen that as the endpoint is furtherly decreased the effect of this phenomenon is reduced and the final quantity of dissolved CO₂ is mainly determined by the CO₂ -brine contact area.

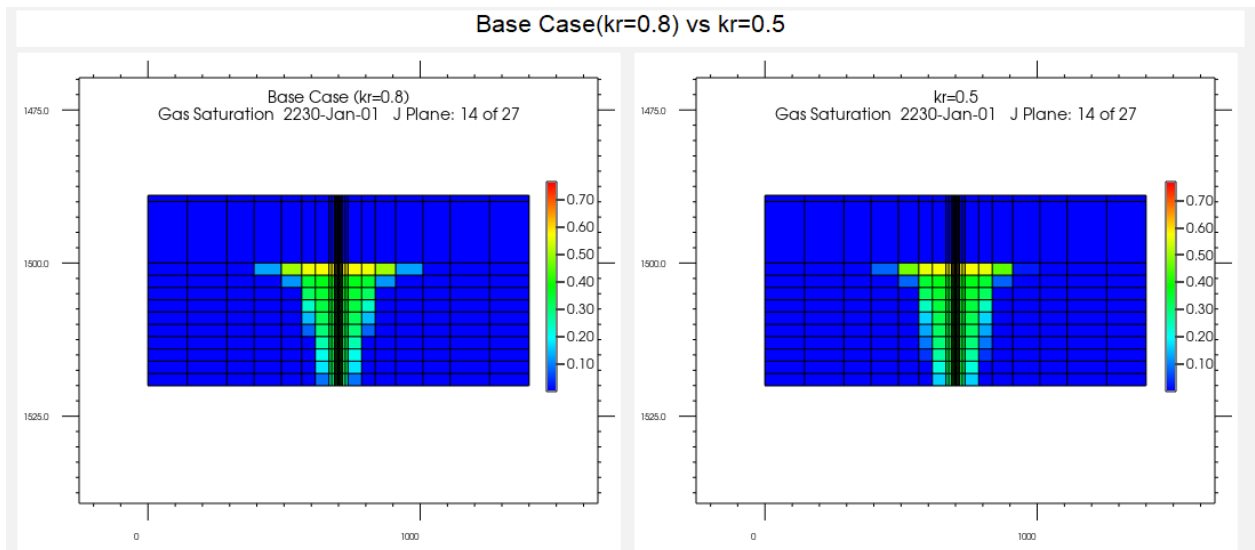


Figure 22: The distribution of the gas saturation at the end of the simulation (200years) for the base case($k_{rCO_2}(S_{wi})=0.8$) (left) and $k_{rCO_2}(S_{wi})=0.5$ (right)

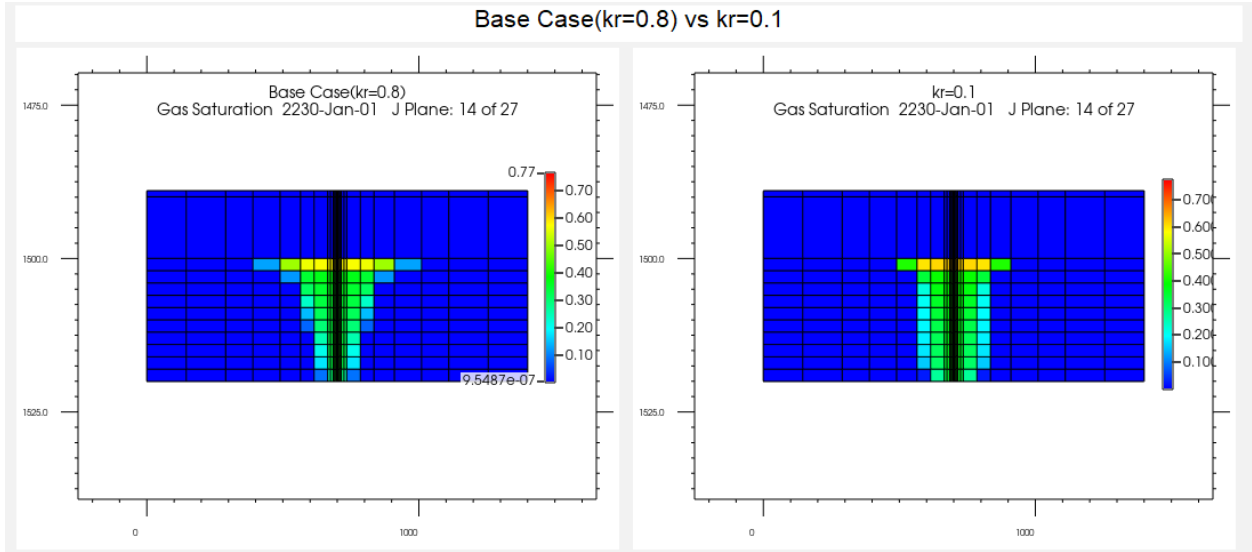


Figure 23: The distribution of the gas saturation at the end of the simulation (200years) for the base case($k_{rCO_2}(S_{wi})=0.8$) (left) and $k_{rCO_2}(S_{wi})=0.1$ (right)

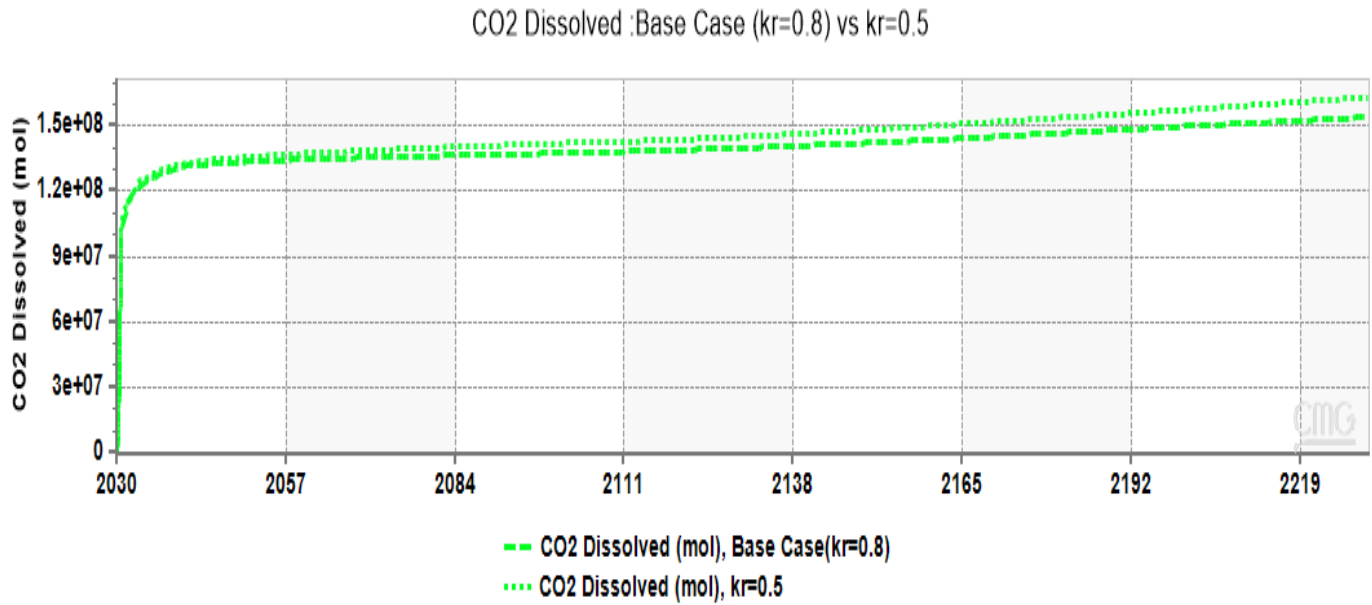


Figure 24: The variation of dissolved CO_2 in function of time for the Base case and for the case($k_{rCO_2}(S_{wi})=0.5$)

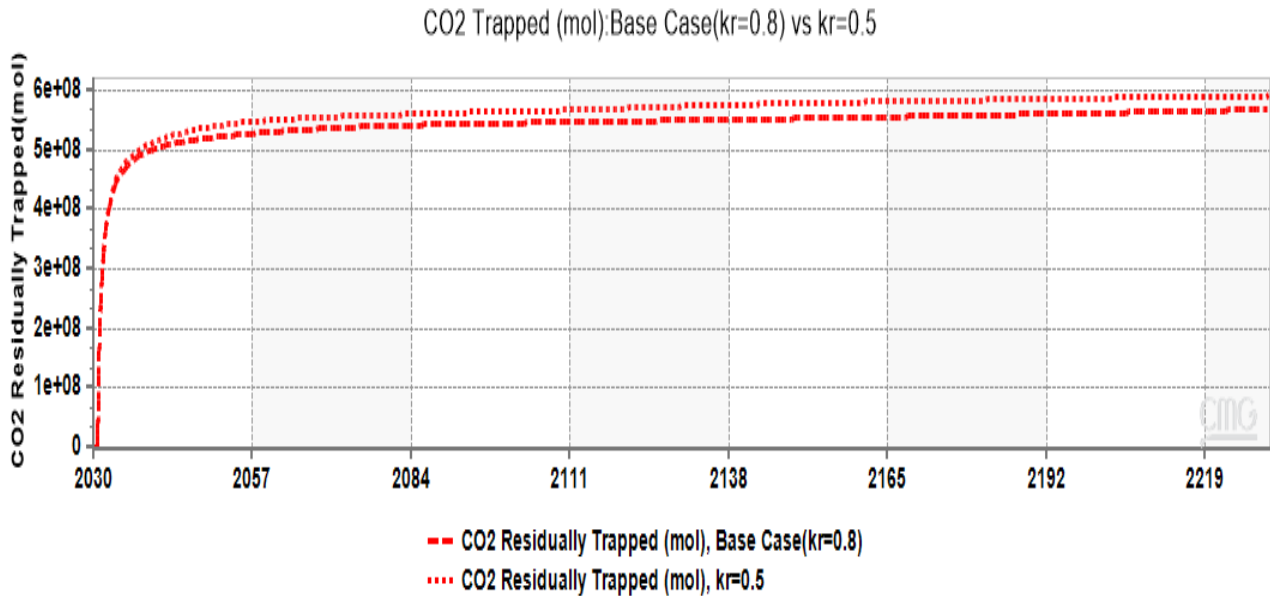


Figure 25: The variation of residually trapped CO₂ in function of time for the Base case and for the case($k_{rCO_2}(S_{wi})=0.5$)

Concerning mineralization, it can be seen that the mineralized share of CO₂ follows the same trend of the dissolved portion, because as mentioned earlier, the dissolution of CO₂ into the brine is considered a precursor to the mineralization of the CO₂. Thus, we can attribute the increase of mineralization of the CO₂ in case where $k_{rCO_2}(S_{wi})=0.5$ to the increase of the dissolution in the same case, and the decrease of mineralization in case where $k_{rCO_2}(S_{wi})=0.1$ to the decrease of the dissolution in that case. Furthermore, the ionic trapping wasn't affected, and the structural trapping decreased as the endpoint was decreased.

6.3 Effect of the Land Coefficient

Three simulations were performed by varying the C coefficient from 0.17 as the lower boundary to 8 as the higher boundary passing by an intermediate value of 3. The simulations' results along with the results from the base case were grouped in table 7.

Table 7: Distribution of CO₂ among the different trapping mechanism for the simulation where C=0.17,3,8 and the base case.

Trapping mechanism	Sim 6 (C=0.17)	Base case C=1.25	Sim 7 (C=3)	Sim 8 (C=8)
	Percentage			
Residual	80.34%	51.94%	29.12%	15.30%
Solubility	10.28%	14.00%	13.93%	17.94%
Ionic	0.02%	0.03%	0.03%	0.03%
Mineral	1.23%	1.50%	1.67%	1.97%
Structural/ Hydrodynamic	8.13%	32.53%	55.25%	64.76%

It can be seen from table 7 the strong relation between the Land coefficient C and the residually trapped percentage of CO₂. This result was expected, because as mentioned in the Land trapping model part (4.4), as C increases the residual trapping efficiency decreases. In fact, going back to the Eq.12, we can clearly see how a higher Land coefficient leads to a lower $S_{CO_2,r}$, which is coherent with the results obtained from the simulations.

In addition, it was observed that the CO₂ dissolved in water and the residually trapped CO₂ are varying in opposite directions. In fact, in the last situation where C=8, the dissolution mechanism is more important than the residual trapping mechanism, as higher quantities of CO₂ were dissolved compared to those residually trapped. That is opposed to what is expected in the simulation timescale, as the residual trapping is expected to be more important than the dissolution trapping mechanism for CO₂ sequestration in the short-term. [5] This in fact shines the light once more on the credibility of the data previously mentioned in the literature.

An explanation for having a more important dissolution trapping with higher Land coefficient can be supported by the fact that, a high Land coefficient, low residual trapping, will facilitate the plume migration. As a consequence, the area of contact between the plume and the CO₂ will increase, which will enhance the dissolution of CO₂ in the brine water. [44] Once more, the mineralization of CO₂ is varying in the same way as the dissolution and this is due to the same reasons mentioned before. As well, the ionic trapping remained the same in all simulations. Finally, the CO₂ structurally trapped is strongly affected by the variation of C and it shows an increasing trend with an increasing C Land coefficient, and this is attributed to the change in residual trapping percentage.

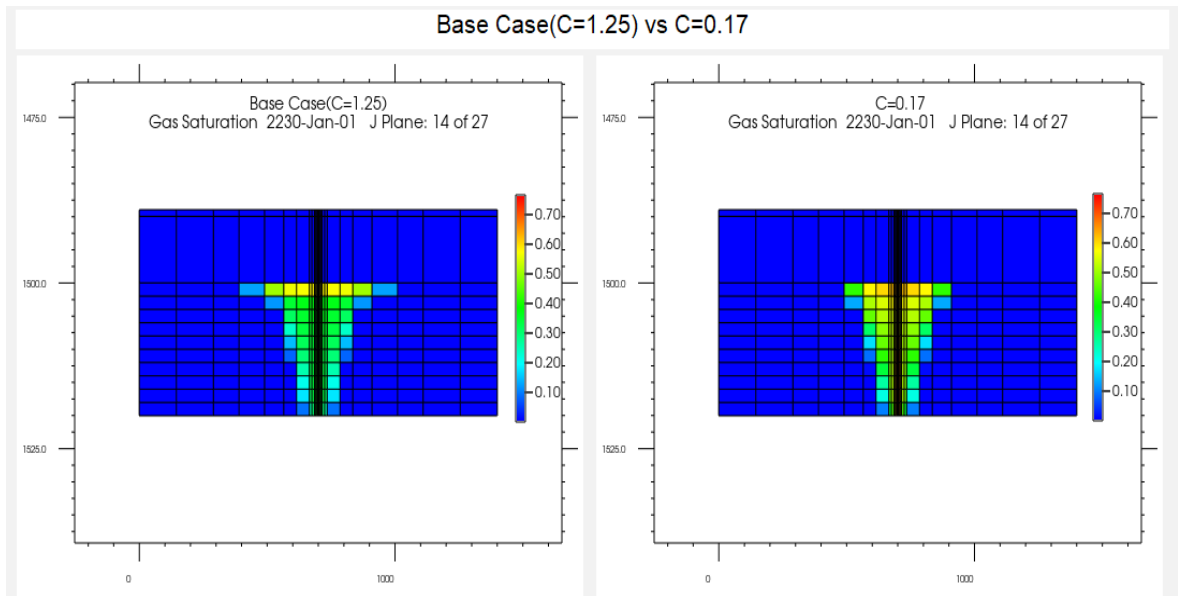


Figure 26: The distribution of the gas saturation at the end of the simulation (200years) for the base case(C=1.25) (left) and C=0.17(right)

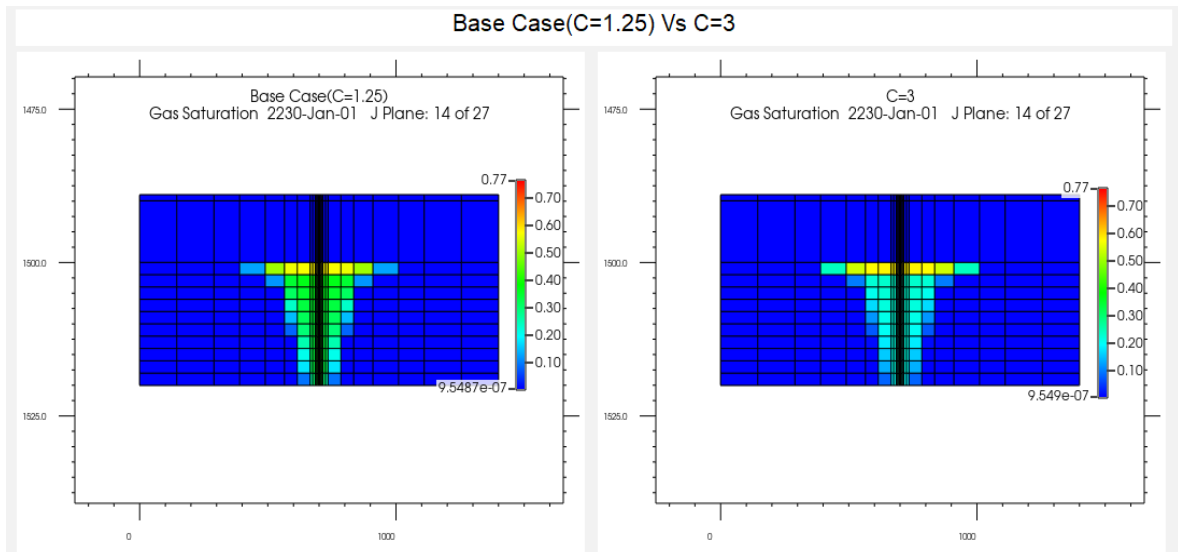


Figure 27: The distribution of the gas saturation at the end of the simulation (200years) for the base case(C=1.25) (left) and C=3(right)

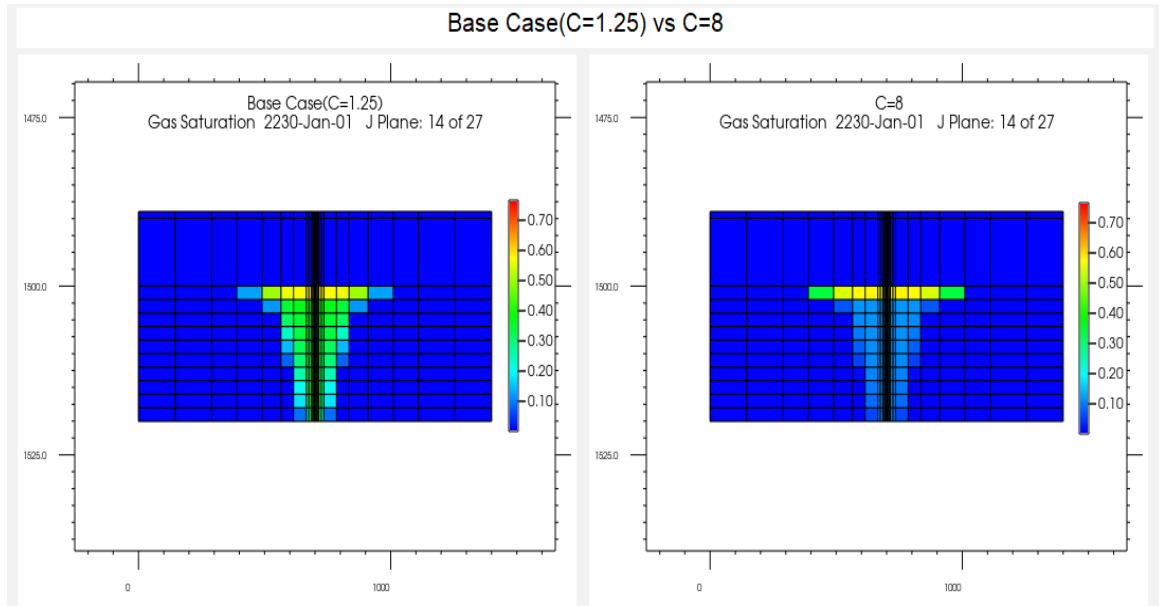


Figure 28: The distribution of the gas saturation at the end of the simulation (200years) for the base case(C=1.25) (left) and C=8(right).

The Fig. (26,27&28) prove exactly what was assumed earlier on, as with the increase of the Land coefficient, the plume tends to migrate entirely upward, as we can see in the picture (Fig.27 and 28). The figures also depict that little amount of gas is being left behind during its ascension due to very low residual trapping at the tail of the plume. As well, the CO₂ plume with high Land coefficient tends to spread more laterally especially in the top layer just under the cap rock, which explains the increase of the dissolution of CO₂ into the brine formation as this was mainly due to the increase of the area of contact between the CO₂ plume and the formation brine. In addition, by inspecting the Fig. (26 & 27), it can be observed that the lower the Land coefficient, the more gas is trapped at lower levels (higher depths), and this is due the fact that while the plume is migrating upward a higher portion of gas is being trapped because of the low Land coefficient. This will lead to low spread of the CO₂ plume at the top layer, which is clearly visible in the picture of C=0.17(Fig.26), as the high portions of CO₂ trapped during the vertical ascension of the plume are no longer available for lateral expansion under the cap rock. Thus the more CO₂ is trapped residually, the less CO₂ is available for migration, thus decreasing the area of contact of CO₂ with the brine, which will eventually reduce the dissolution mechanism.

However, the Land coefficient cannot be modified as it is a property of the rock-pore structure making it specific to reservoir, as it depends on clay percentage, micro porosity, permeability, brine composition and CO₂. [74] [44] In fact, as the absolute permeability decreases, the C Land coefficient increases, which leads to a decrease in trapping. [41]

6.4 Effect of Capillary pressure

The effect of the capillary pressure was studied by performing three simulations. The first simulation was performed without any capillary pressure, in the second the imbibition capillary curve was opted out, and the third simulation was performed by increasing the P_c to 8.27 kPa. Table 8 summarizes the results of different simulations when altering the capillary pressure curves.

Table 8: Distribution of CO₂ among the different trapping mechanism for the different capillary pressure curves.

Trapping mechanism	Sim 9 (without P_c)	Base Case($P_c=3.7$)	Sim 10 (no P_c^i)	Sim 11 ($P_c=8.27$)
	Percentage			
Residual	44.41%	51.94%	57.36%	45.74%
Solubility	11.61%	14.00%	14.47%	15.02%
Ionic	0.02%	0.03%	0.03%	0.03%
Mineral	1.33%	1.50%	1.52%	1.60%
Structural/ Hydrodynamic	42.63%	32.53%	26.62%	37.61%

First, let's look at the case where no capillary pressure curves were included in the simulation. The results show that all the trapping mechanisms have been affected negatively (decrease in percentage) but in different proportions. The highest change was observed in the residual trapping share, as the portion of CO₂ residually trapped was reduced significantly from 51.94% (Base Case) to 44.41%. In this simulation, the residual trapping is only affected by the relative permeability hysteresis since no capillary pressure curves were taken into account. Looking at the Fig.29 of the gas saturation distribution when no capillary pressure was included, it can be seen that the top layer has reached irreducible water saturation once the plume has reached its final upward destination and remained stable till the end of the simulation. This can be traced back to the absence of entry capillary pressure which renders the upward migration easier and faster than the base case scenario. Having a higher saturation in the top layer is behind the lower residual trapping since it is considered harder to residually trap in the top layer. [37] [75] This can be proved by inspecting the distribution of the residual CO₂ distribution in Fig.30 as it can be seen that no CO₂ was trapped in the top layer and this is because the water was at irreducible water saturation, thus incapable of trapping the CO₂ by the snap-off mechanism.

On another hand, it was observed that the lateral migration of the CO₂ plume is more important in the base case than in the case in which no P_c was included. This can be attributed to the fact that the omission of capillary pressure led to a stagnant plume, as it didn't expand laterally after the halt of the injection. This has resulted in a lower area of contact between the two phases, which explains the lower CO₂ dissolution in simulation 9 that eventually led to a lower mineralization. In addition, the ionic trapping mechanism is considered to be unaffected by the omission of the capillary pressure curves.

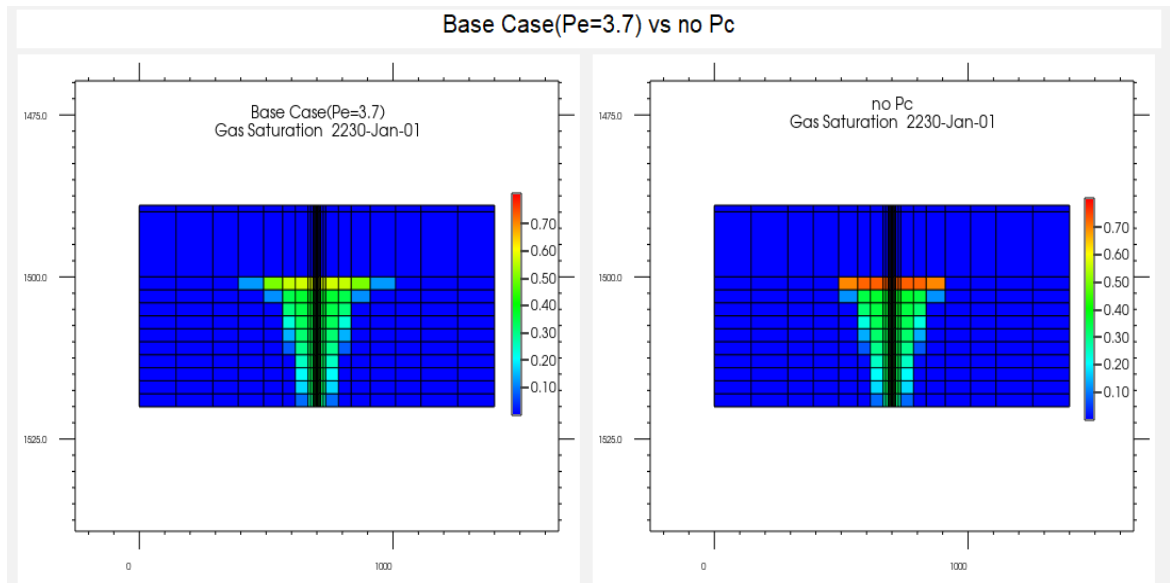


Figure 29: The distribution of the gas saturation at the end of the simulation (200years) for the Base case(left) and the case where P_c was not included (right).

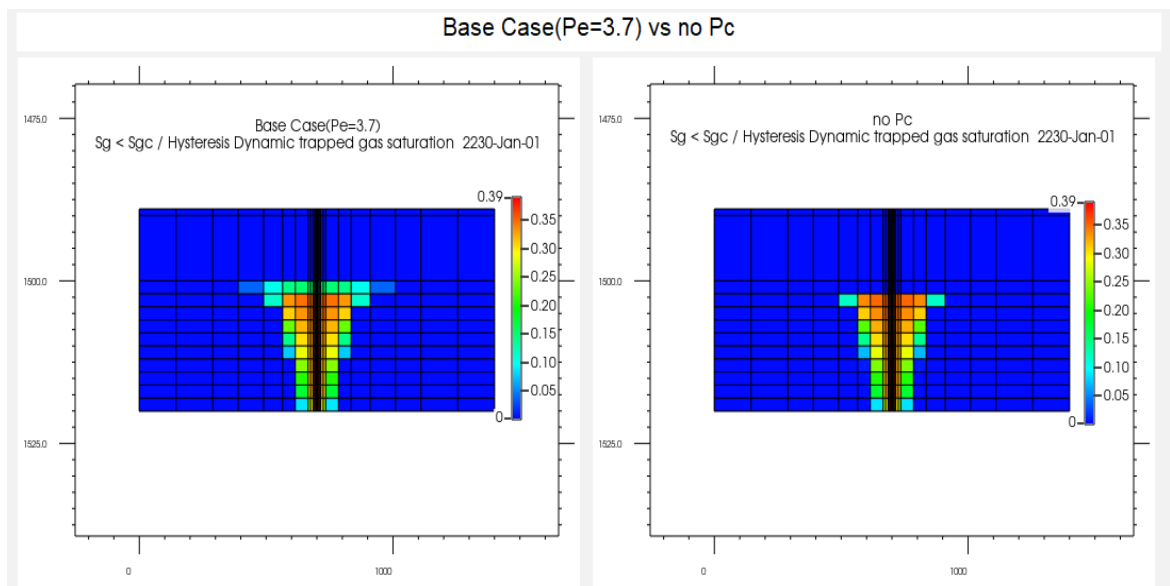


Figure 30: The distribution of the residually trapped saturation of CO₂ at the end of simulation time (200 years) for the Base case(left) and the case where P_c was not included (right).

Second, let us discuss the effect of excluding hysteresis in the capillary pressure curves. In the case where only the drainage capillary pressure was included, it can be seen that the residual CO₂ trapped increases and that is due to the fact that without including capillary

hysteresis the residual trapping is being overestimated as mentioned by [42] [76]. In fact, during the snap-off mechanism the capillary pressure decreases and in this case it will reach a threshold pressure which is on the drainage curve since no hysteresis was included. This threshold is higher than what it would have been if the imbibition capillary curve was included. This is leading to a higher residual trapping under the cap rock (see Fig.31). Furthermore, the slight increase in the mineralization can be attributed to the slight increase in the dissolved part of the trapped CO₂. However, there was no change in the ionic trapping.

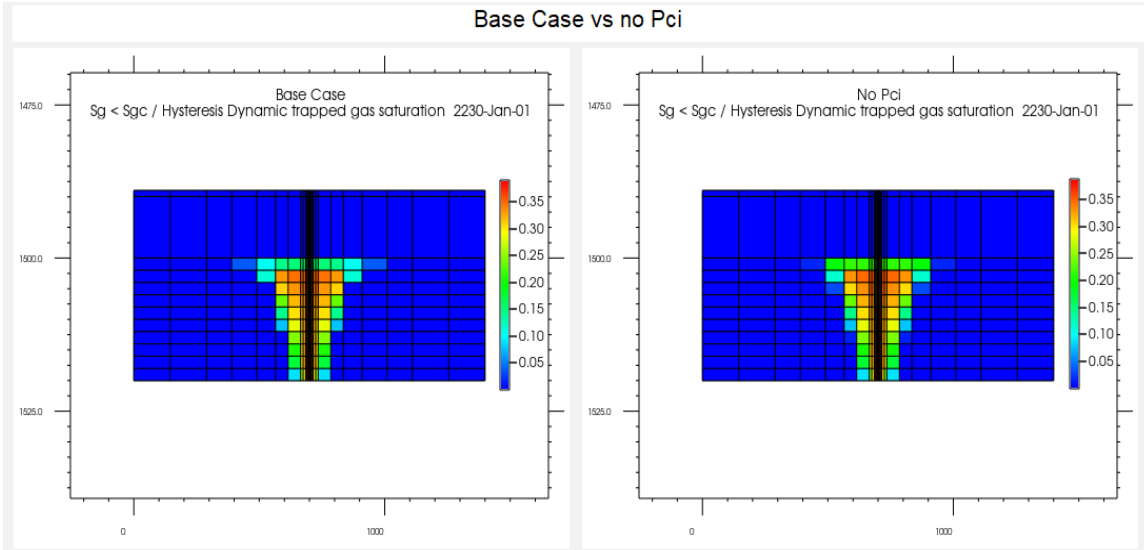


Figure 31: Figure showcasing the distribution of the residually trapped CO₂ at the end of the simulation (200 years) for the base case (left) and for the case where no capillary pressure hysteresis was included (right)

Third, concerning the case where the entry capillary pressure P_e was increased with respect to the base case, the results show that increasing the entry capillary pressure leads to lower residually trapped CO₂. This can be explained by comparing the imbibition capillary pressure curves for the base case and for the case in which the entry capillary pressure was increased (see Fig.32). The latter curve is steeper than the one the base case. This means that the brine in the high capillary pressure case has to overcome a higher pressure in order to imbibe the CO₂ and trap it according to the snap-off mechanism, which led to an increase in the difficulty to residually trap the CO₂. This can also be proved by inspecting the Fig.33 where it can be seen that the residual trapping at the top layer is significantly lower in the case of higher entry capillary pressure.

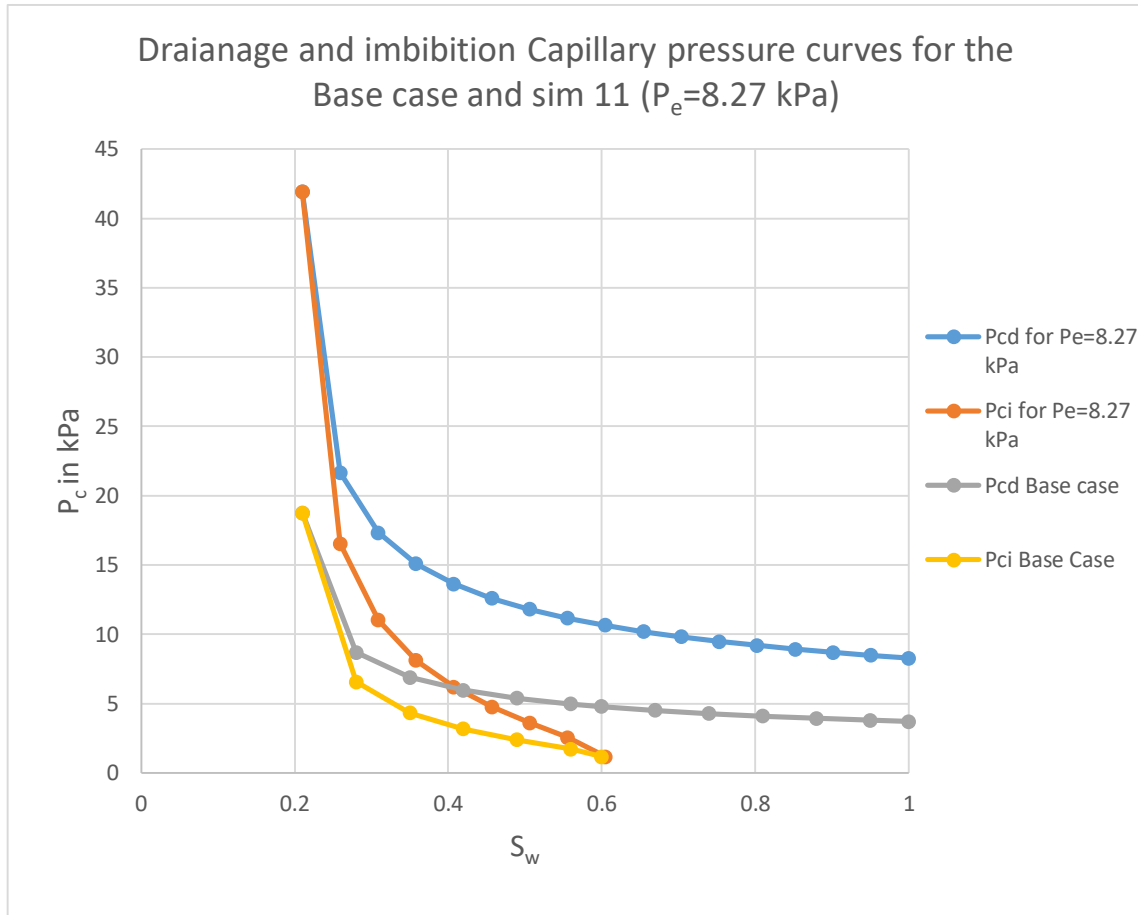


Figure 32: Plot of the drainage and imbibition capillary pressure curves for the base case and the simulation where $P_e=8.27$ kPa.

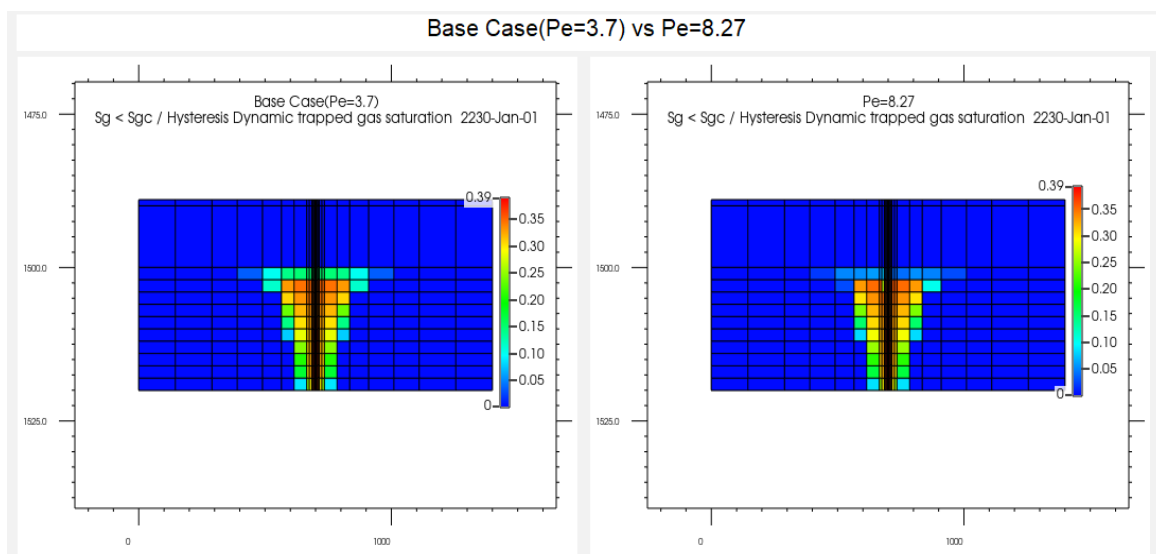


Figure 33: The distribution of saturation of residually trapped CO_2 at the end of simulation time (200 years) for the Base case(left) and the simulation where $P_e=8.27$ kPa (right).

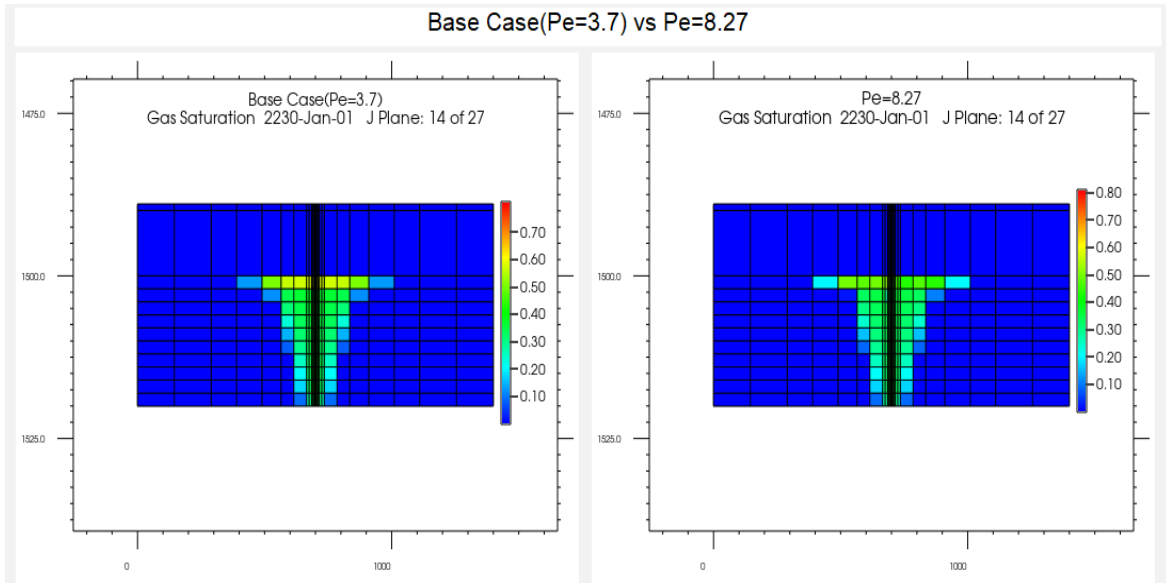


Figure 34: The CO₂ saturation at the end of the simulation (200 years) for the base case (left) and simulation where $P_e=8.27$ kPa (right)

As well inspecting the Fig.34, it can be seen that the plume size is almost the same with the only difference in the most extreme cell of the CO₂ plume in the top layer that shows a higher saturation of CO₂, which explains the reason behind the slight increase of the CO₂ dissolution in brine in the simulation 11 with respect to the base case. In fact, the increase of dissolution with an increase of capillary pressure is also encountered by [77].

As mentioned in the previous parts, the mineralization follows the dissolution and this case is no exception, as also a slight increase was observed between the two cases. Finally, the ionic trapping was not affected by the increment of the entry capillary pressure.

However, it was expected that with the increase of the capillary pressure curves, the increase of the capillary forces will lead to an increase in the residual trapping. The contradiction can be attributed to the fact that during the simulations the term P_s in the imbibition curve equation Eq.27 was not varied, due to lack of data in the literature, when the P_e is increased. Therefore, this resulted in a decrease in the residual trapping.

The variation of the structural trapping is in such a way opposite to the variation of the residual trapping since the variation of the latter is the dominant between the different cases when the capillary pressure curves were altered. Therefore, the structural trapping was reduced when the capillary pressure was introduced with respect to no capillary pressure. In addition, it was once more reduced with the omission of the imbibition capillary curve. However, it was increased when the entry pressure curve was increased.

6.5 Effect of Corey Coefficient

Since Corey exponents reflect the wettability and IFT, it was decided that in each simulation in the sensitivity analysis only one exponent is varied, either the one of the water or the one of CO₂.

The relative permeability curves for the different Corey exponents are represented in Fig.35 and 36, and the results of the simulations from varying Corey exponents are grouped in table 9.

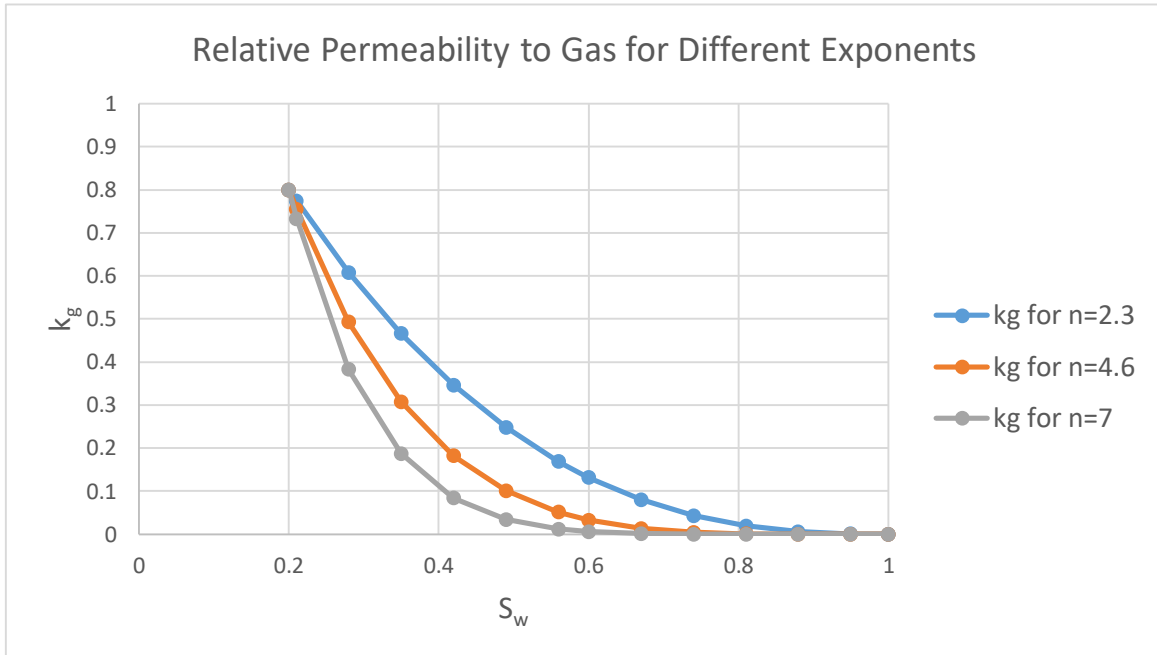


Figure 35:Relative permeability to CO₂ for different Corey exponents.

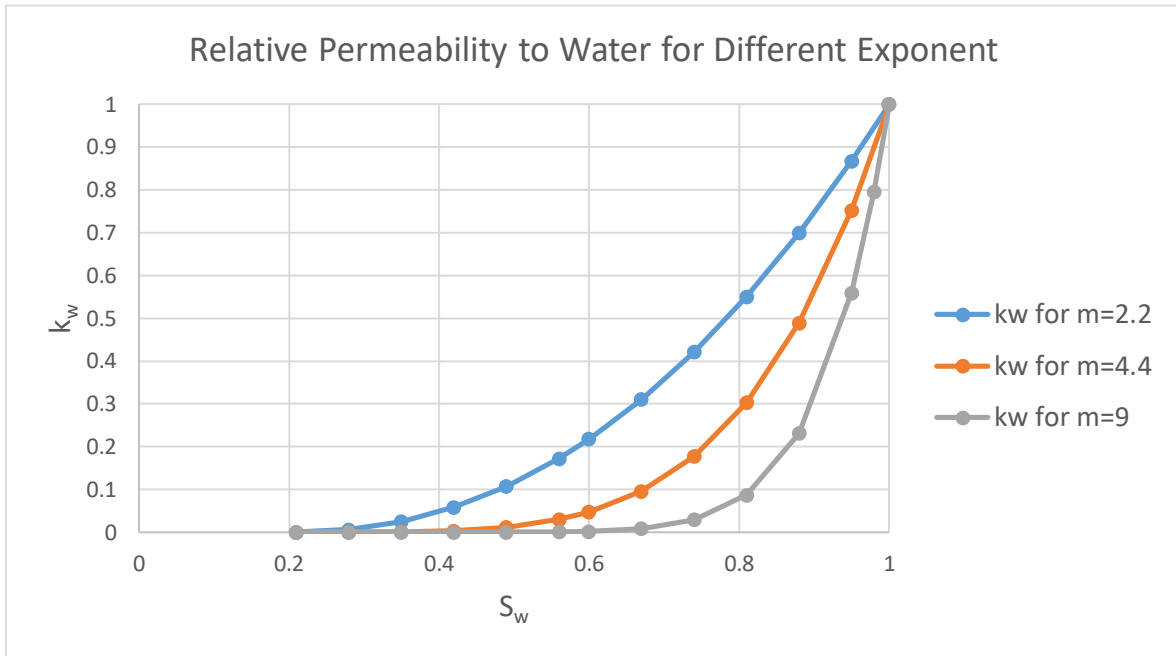


Figure 36: Relative permeability to water for different Corey exponents.

Table 9: Distribution of CO₂ among the different trapping mechanism for the different Corey exponents.

Trapping mechanism	Sim 12 (m=2.2; n=4.6)	Sim14 (m=4.4;n=2.3)	Base Case (m=4.4; n=4.6)	Sim 13 (m=9;n=4.6)	Sim 15 (m=4.4; n=7)
	Percentage				
Residual	41.97%	42.53%	51.94%	57.87%	48.48%
Solubility	11.64%	14.04%	14.00%	17.17%	13.71%
Ionic	0.03%	0.03%	0.03%	0.03%	0.03%
Mineral	1.45%	1.60%	1.50%	1.75%	1.48%
Structural/ Hydrodynamic	44.92%	41.80%	32.53%	23.18%	36.31%

First, let's start to analyze the residually trapped quantity. The reduction of the Corey exponent for the water phase will shift the relative permeability to water up as the curve becomes more linear (Fig.36). In this case, the gas was able to easily reach the top layer as the drainage of the water was facilitated. Since a good portion of the gas was able to reach the top layer during the injection, this renders the residual trapping of the gas more difficult, which explains the lower residual trapping of CO₂. [75] [37] As well, since the brine exponent is now lower the relative permeability curves represent a less water-wet system, which is an unfavorable condition for the snap-off phenomenon.

In addition, it was also observed that a substantial amount of CO₂ reached the top layer when the CO₂ exponent was decreased (Fig.38), but this time it was due to the increase in

the relative permeability to CO₂ (Fig.35). As mentioned earlier, having a significant part of the gas in the top layer increases the difficulty of the residual trapping, which explains the result obtained. Conversely, the lower residual trapping when increasing the CO₂ exponent can be attributed to the lower plume migration as the saturation distribution is more uniform (Fig.39).

When the brine exponent is increased to its maximum value, it was observed that the share of the residual trapping increases. This is expected as the increase of the brine Corey exponent represents a more water-wet medium, which is favorable for the occurrence of the snap-off. This can explain the high residual trapping observed when brine Corey exponent is increased.

When the brine exponent was reduced the most significant reduction of the dissolution of CO₂ was obtained. Although in that particular case there is a significant plume spreading at the top, that isn't enough to compensate the lower surface of contact between the two phases along the vertical direction that is present in the base case Fig.37. When the CO₂ exponent is reduced to the half of the base case, an equal dissolution as in the base case was obtained. In this case, the CO₂ is largely concentrated in the top layer and have an important lateral expansion due to the increase in the relative permeability to CO₂, which was able to compensate the lower area of contact along the vertical direction Fig.38. On the contrary, in the case where the CO₂ exponent is maximum, the lower relative permeability to CO₂ led to having a more compact plume that has a more important area of contact along the vertical direction. However, this wasn't enough to match the area of contact present in the base case and as a result the dissolved CO₂ is slightly lower Fig.39. Considering now the last case, where the brine Corey exponent was maximized, it was observed that this resulted in a higher dissolved portion than the base case. In this case, the reduced relative permeability to water led to a more uniform distribution of the CO₂ plume in the vertical direction Fig.40. This time the vertical area of contact between the two phases was higher and exceeded the total area of contact of the base case. Thus, the increase in the dissolved quantity is related to a higher contact area of the CO₂ plume with the formation brine.

Moreover, the mineralization also followed the same trend of the dissolution for the same reasons mentioned before. Whereas, the ionic trapping remained unchanged for the different Corey exponents.

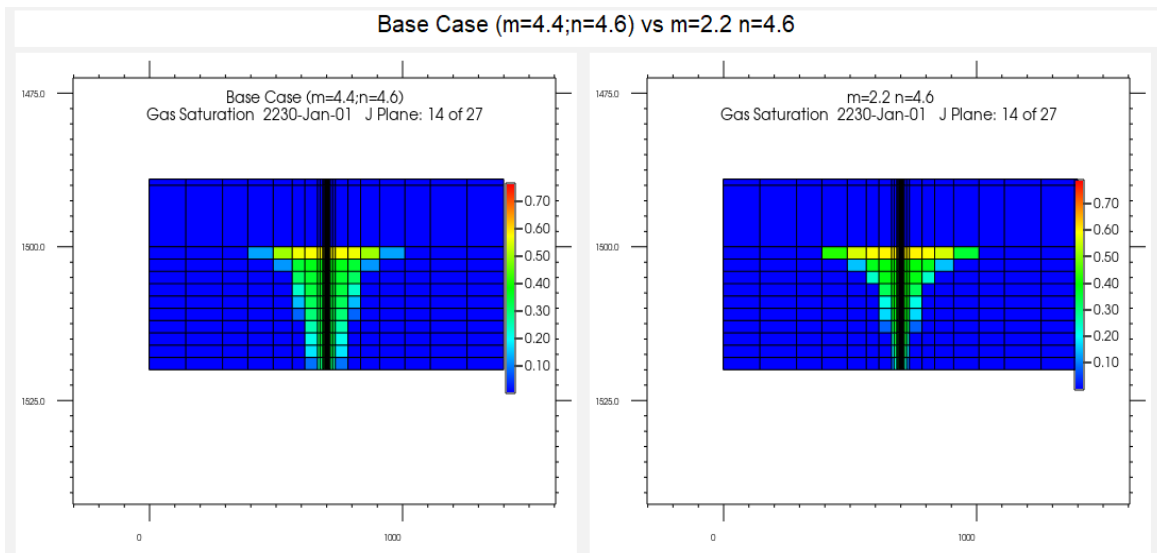


Figure 37: The distribution of the gas saturation at the end of the simulation (200years) for the base case($m=4.4;n=4.6$) (left) and sim12 ($m=2.2;n=4.6$) (right)

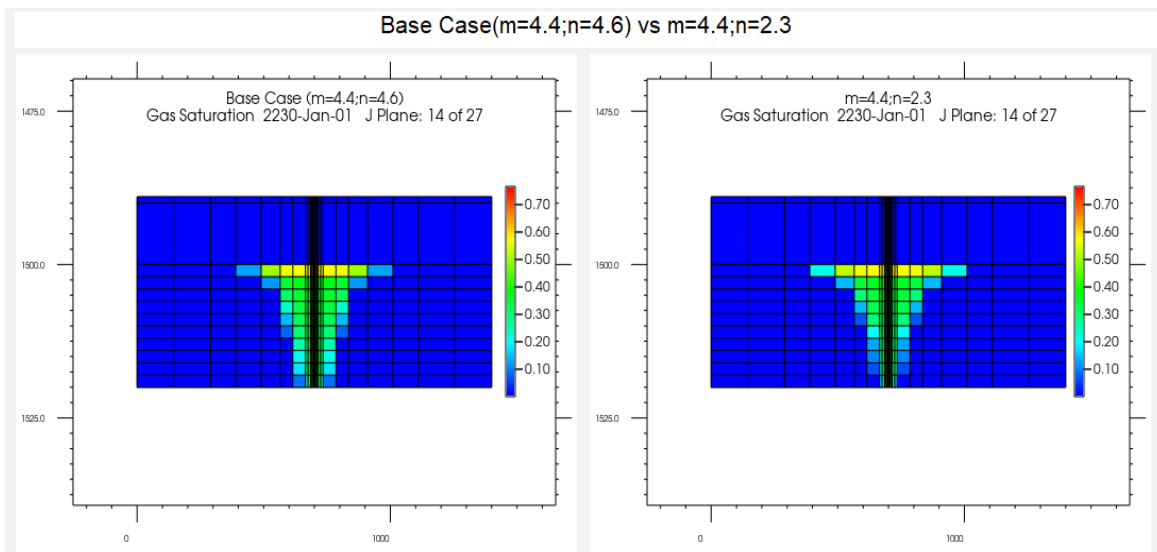


Figure 38: The distribution of the gas saturation at the end of the simulation (200years) for the base case($m=4.4;n=4.6$) (left) and sim14 ($m=4.4;n=2.3$) (right)

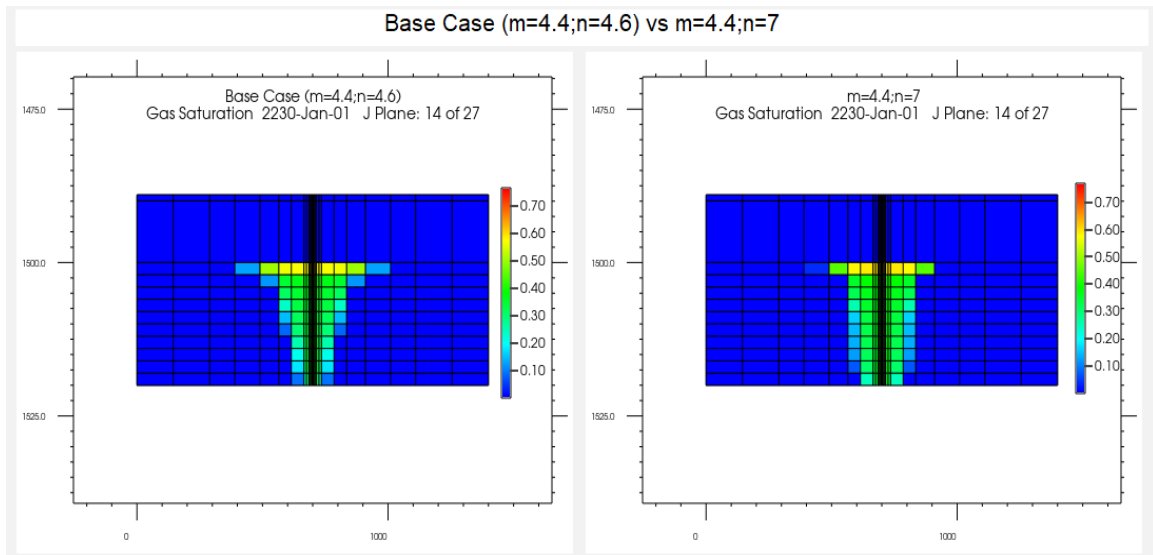


Figure 39: The distribution of the gas saturation at the end of the simulation (200years) for the base case($m=4.4;n=4.6$) (left) and sim15 ($m=4.4;n=7$) (right)

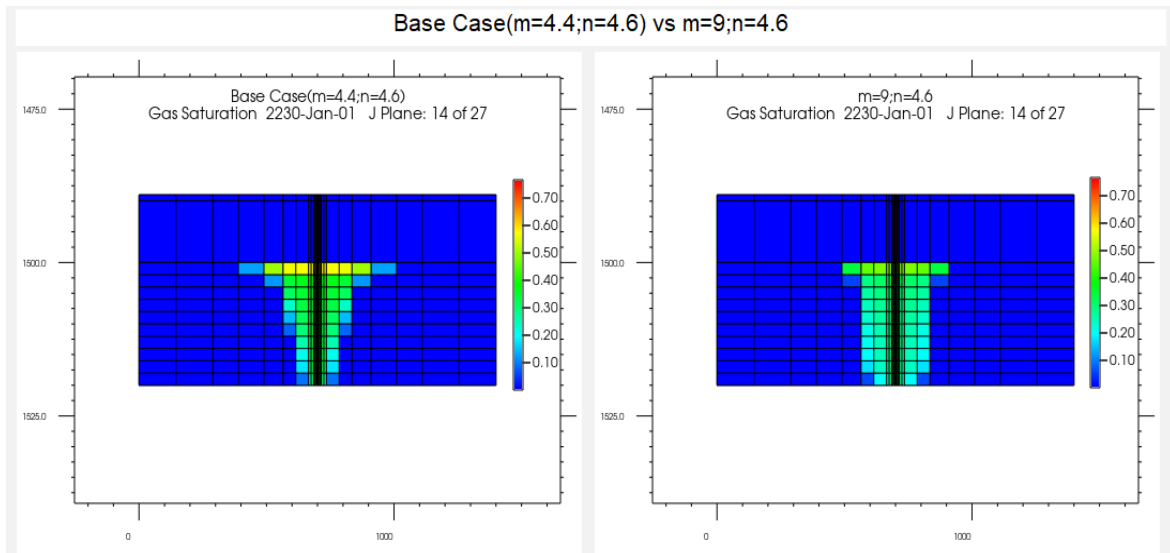


Figure 40: The distribution of the gas saturation at the end of the simulation (200years) for the base case($m=4.4;n=4.6$) (left) and sim13 ($m=9;n=4.6$) (right)

7 Conclusion

In this study a sensitivity analysis on all parameters affecting the relative permeability and capillary pressure curves was performed and their impact on the final CO₂ storage was investigated. To be able to accomplish this task, the lowest and highest boundary were identified based on the literature review, and the Bentheimer formation was adopted as the base case.

The simulation time was chosen to be 200 years, as it was believed that this period was enough to monitor the effects of relative permeability on the different storage mechanisms. The sensitivity analysis was performed by changing only one of the following parameters at a time: irreducible water saturation (S_{wi}), endpoint of the relative permeability to CO₂ ($k_{rCO_2}(S_{wi})$), Land Coefficient C, capillary entry pressure (P_e), and Corey exponents.

The results of the sensitivity analyses showed that the Land coefficient had the most important impact on the CO₂ plume size, migration and trapping. This is aligned with the results found in technical literature [78]. By decreasing the Land Coefficient, it was found that an increase in residual trapping occurs at the expense of solubility and structural trapping.

However, the Land coefficient is considered an intrinsic property of the formation, and according to literature [42] it falls between $1 < C < 2$ for prospective storage formations.

The sensitivity analysis on irreducible water saturation showed an increased residual, solubility, and mineralization trapping for an increase in irreducible water saturation. Thus a high irreducible water saturation corresponds to high storage security as a lower portion of the CO₂ is structurally trapped, which is the portion that is more susceptible to a potential risk of leaking through the cap rock.

The variation of the endpoint of the relative permeability to CO₂ had a limited effect on the variation of the trapping distribution among the different mechanisms. It showed an increase in residual trapping for a decrease in the endpoint relative permeability. However, no obvious trend exists for the solubility and mineralization trapping. Nonetheless, we expect to have in practice a high endpoint of the relative permeability, in the range of $k_{rCO_2}(S_{wi})=0.5-1$, as the CO₂ is the non-wetting fluid [21].

Performing the simulations without capillary pressure forces led to an underestimation of the residual, solubility and mineralization trapping mechanisms. However, opting out only the imbibition capillary curve overestimates the residually trapped CO₂. In addition, increasing the capillary entry pressure led to a decrease in residual trapping and an increase in solubility trapping.

The sensitivity analysis performed on Corey exponents showed that an increase in Corey exponents for the brine will increase residual and dissolution trapping. Whereas, reducing CO₂ Corey coefficient led to a decrease in residual trapping due to the increased quantity of gas in the top layer where it's more difficult to residually trap. As well, an increase in CO₂ Corey exponent also leads to lower residual trapping and this was due to lower plume

migration. Moreover, an increase in the Corey exponents whether for the brine or the CO₂ led to a more compact plume.

Furthermore, the sensitivity analysis confirmed the entanglement present between the mineralization and the dissolution of CO₂, as it was observed that in all the simulations the quantity trapped by these two mechanisms varied in the same direction. The reason behind this was mainly attributed to the fact that the dissolution of CO₂ is a necessary step in the CO₂ mineralization process. Nonetheless, the mineralization variation throughout all the sensitivity analysis was limited and resulted in a trapping share lower than 5%. In order to observe a significant portion of the CO₂ mineralized, the timescale of the simulation should be increased to make it compatible with the mineralization time scale.

Finally, ionic trapping seems unaffected by all the variations done on the relative permeability and capillary pressure curves. The ionic trapping had the smallest share of all trapping mechanisms, which was also the case in paper. [78] In fact, as mentioned by [10], the ionic trapping is a function of the pH of the solution, and in the performed simulations the pH was always lower than the range (pH>6) where the ionic trapping is more important.

8 References

- [1] Susan Solomon, John S. Daniel, Todd J. Sanford, Daniel M. Murphy, Gian-Kasper Plattner, Reto Knutti, and Pierre Friedlingstein, "Persistence of climate changes due to a range of greenhouse gases," *PNAS*, vol. 107, no. 43, 2010.
- [2] UN, "United In Science 2021: A multi-organization high-level compilation of the latest climate science information," World Meteorological Organization, 2021.
- [3] IEA, "IEA," April 2021. [Online]. Available: <https://www.iea.org/reports/about-ccus>.
- [4] IEA, "Net Zero by 2050," 2021.
- [5] IPCC, "Carbon Dioxide Capture and Storage," Cambridge University Press, 2005.
- [6] Sara Budinis , "IEA," November 2021. [Online]. Available: <https://www.iea.org/reports/direct-air-capture>.
- [7] Paweł Madejski , Karolina Chmiel, Navaneethan Subramanian and Tomasz Ku's , "Methods and Techniques for CO2 Capture: Review of Potential Solutions and Applications in Modern Energy Technologies," *Energies*, no. 15, 2022.
- [8] Temitope Ajayi, Jorge Salgado Gomes & Achinta Bera, "A review of CO2 storage in geological formations emphasizing modeling, monitoring and capacity estimation approaches," *Petroleum Science*, no. 16, October 2019.
- [9] J. P. M. PhD, "Summary of Carbon Dioxide Enhanced Oil Recovery (CO2EOR) Injection Well Technology," American Petroleum Institute, Texas.
- [10] S. A. Rackley, "Introduction to geological storage," in *Carbon Capture and Storage*, Elsevier Science, 2009, p. 675.
- [11] Pierre Cerasi, Jelena Todorovic, Martin Raphaug and Alv-Arne Grimstad., "Sintef," 12 October 2021. [Online]. Available: <https://blog.sintef.com/sintefenergy/ccs/salt-precipitation-experiments-for-improved-co2-storage/>. [Accessed June 2022].
- [12] L.G.H. (Bert) van der Meer, Cor Hofstee, Bogdan Orlic, "The fluid flow consequences of CO2 migration from 1000 to 600 metres upon passing the critical conditions of CO2," *Energy Procedia*, pp. 3213-3220, 2009.
- [13] Christian Hermanruda*, Terje Andresena, Ola Eikena, Hilde Hansena, Aina Janbua, Jon Lipparda, Hege Nordgård Bolåsa, Trine Helle Simmenesa, Gunn Mari Grimsmo Teigea, Svend Østmo, "Storage of CO 2 in saline aquifers—Lessons learned from 10 years of injection into the Utsira Formation in the Sleipner area," *Energy Procedia*, vol. 1, pp. 1997-2004, 2009.
- [14] Dongxiao Zhang*, Juan Song, "Mechanisms for geological carbon sequestration," *Procedia IUTAM*, vol. 10, p. 319 – 327, 2014.
- [15] Stefan Bachu W.D. Gunter E.H. Perkins, "Aquifer disposal of CO2: Hydrodynamic and mineral trapping," *Energy Conversion and Management*, vol. 35, no. 4, pp. 269-279, 1994.
- [16] M. RASMUSSEN, "Residual and Solubility trapping during Geological CO2 storage," 2018.
- [17] S. Rackley, "Geochemical and biogeochemical," in *Carbon Capture and Storage features, events, and processes*, Elsevier Science & Technology, 2009, pp. 365-385.
- [18] Perkins, E, Czernichowski-Lauriol, I, Azaroual, M, Durst, P, "Long term predictions of CO2

- storage by mineral and solubility trapping in the Weyburn Midale Reservoir," in *Proceedings of the 7th international conference on greenhouse gas control technologies*, 2004.
- [19] Kampman N, Bickle M, Wigley M, Dubacq B, "Fluid flow and CO₂-fluid-mineral interactions during CO₂-storage in sedimentary basins," *Chem Geol*, vol. 369, p. 22–50, 2014.
- [20] Jean-Christophe Perrin · Sally Benson, "An Experimental Study on the Influence of Sub-Core Scale Heterogeneities on CO₂ Distribution in Reservoir Rocks," *Springer*, 2009.
- [21] S. K. Catriona Reynolds and R. P. Sally Benson, "Relative Permeability Analyses to Describe Multi-Phase Flow in CO₂ Storage Reservoirs," GCCSI, 2012.
- [22] Sally M. Benson, Ferdinand Hingerl, Lin Zuo, Ronny Pini, Sam Krevor Catriona Reynolds, Ben Niu, Ran Calvo And Auli Niemi, "Relative Permeability for muti-phase flow for CO₂ storage reservoirs:PartII Resolving fundamental issues and filling data gaps," GCCSI, 2015.
- [23] J. Levine, *Relative Permeability Experiments of Carbon Dioxide Displacing Brine & Their Implications for Carbon Sequestration*, Columbia University, 2011.
- [24] Muhammad Aslam Md Yusof, Yen Adams Sokama Neuyam, Mohamad Arif Ibrahim, Ismail M. Saaid, Ahmad Kamal Idris and Muhammad Azfar Mohamed , "Experimental study of CO₂ injectivity impairment in sandstone due to salt precipitation and fines migration," *Journal of Petroleum Exploration and Production Technology*, 2022.
- [25] H. H. Rohaldin Miri*, "Salt precipitation during CO₂storage—A review," *Journal of Green house Gas Control*, vol. 51, pp. 136-147, 2016.
- [26] Liu, Hui-Hai; Zhang, Guoxiang; Yi, ZhenLian; Wang, Yingxue, "A permeability-change relationship in the dryout zone for CO₂ injection into saline aquifers," *International Journal of Greenhouse Gas Control*, vol. 15, pp. 42-47, 2013.
- [27] Miri, Rohaldin; van Noort, Reinier; Aagaard, Per; Hellevang, Helge, "New insights on the physics of salt precipitation during injection of CO₂ into saline aquifers.," *International Journal of Greenhouse Gas Control*, vol. 43, p. 10–21, 2015.
- [28] J. R. Fanchi, "Measures of Rock-Fluid Interactions," in *Shared Earth Modeling*, 2002, pp. 108-132.
- [29] P. B. Jordan, *Two-Phase Relative Permeability Measurements in Berea Sandstone at Reservoir Conditions*, The University of Texas at Austin, 2016.
- [30] Li, X., E.S. Boek, G.C. Maitland, J.P.M. Trusler, " Interfacial Tension of (Brines +CO₂): CaCl₂(aq), MgCl₂(aq), and Na₂SO₄(aq) at Temperatures between (343 and 423) K, Pressure between (2 and 50 MPa), and Molalities of (0.5 to 5) mol·kg⁻¹," *Journal of Chemical and Engineering Data*, vol. 57, pp. 1369-1375, 2012.
- [31] V.P. Dimri, R.P. Srivastava, Nimisha Vedanti, *Fractal Models in Exploration Geophysics*, ELSEVIER, 2012.
- [32] M. T. v. Genuchten, "A Closed-form Equation for Predicting the Hydraulic Conductivity of Unsaturated Soils," *Soil Science Society of America Journal*, vol. 44, no. 5, pp. 892-898, 1980.
- [33] R. H. Brooks and A. T. Corey, *Hydraulic Properties of Porous Media*, Colorado State University, 1964.
- [34] Boxiao Li, Hamdi A. Tchelepi, Sally M. Benson, "Influence of capillary-pressure models on CO₂ solubility trapping," *Advances in Water Resources*, vol. 62, p. 488–498, 2013.

- [35] *. M. W. S. P. S. K. S. M. M. Oostroma, "Comparison of relative permeability–saturation–capillary pressure models for simulation of reservoir CO₂ injection.," *International Journal of Greenhouse Gas Control*, vol. 45, pp. 70-85, 2016.
- [36] Elizabeth J. Spiteri, Ruben Juanes, "Impact of relative permeability hysteresis on the numerical simulation of WAG injection," *Journal of Petroleum Science and Engineering*, vol. 50, pp. 115-139, 2006.
- [37] R. Juanes, E. J. Spiteri, F. M. Orr Jr., M. J. Blunt, "Impact of relative permeability hysteresis on geological CO₂ storage," *Water Resources*, vol. 42, no. 12, 2006.
- [38] de Gennes, P.-G., F. Brochard-Wyart, and D. Quere, "Hysteresis and Elasticity of Triple Lines," in *Capillarity and Wetting Phenomena: Drops, Bubbles, Pearls, Waves*, New York, Springer, 2004, pp. 69-85.
- [39] L. CARLON S, *Calculation of Imbibition Relative Permeability for Two- and Three-Phase Flow From Rock Properties*, 1942.
- [40] Ben Niu, Ali Al-Menhali, and Samuel C. Krevor, "R. Juanes, E. J. Spiteri, F. M. Orr Jr., M. J. Blunt," *Water Resources*, vol. 51, pp. 2009-2029, 2015.
- [41] Samuel C. M. Krevor, Ronny Pini, Lin Zuo, and Sally M. Benson, "Relative permeability and trapping of CO₂ and water in sandstone rocks at reservoir conditions," *Water Resources Research*, vol. 48, 2012.
- [42] Catrin Harris, Samuel J. Jackson, Graham P. Benham, Samuel Krevor, Ann H. Muggeridge, "The impact of heterogeneity on the capillary trapping of CO₂ in the Captain Sandstone," *International Journal of Greenhouse Gas Control*, vol. 112, 2021.
- [43] N.M. Burnside, M. Naylor, "Review and implications of relative permeability of CO₂/brine systems and residual trapping of CO₂," *International Journal of Greenhouse Gas Control*, vol. 23, pp. 1-11, 2014.
- [44] Samuel Krevor, Martin J. Blunt, Sally M. Benson, Christopher H. Pentland, Catriona Reynolds, Ali Al-Menhali, Ben Niu, "Capillary trapping for geologic carbon dioxide storage – From pore scale physics to field scale implications," *International Journal of Greenhouse Gas Control*, 2015.
- [45] Cut Aja Fauzia, Ahmed Al-Yaseri, Emad Al-Khdheawi, Nilesh Kumar Jha, Hussein Rasool Abid, Stefan Iglauer, Christopher Lagat and Ahmed Barifcani, "Effect of CO₂ Flooding on the Wettability Evolution of Sand-Stone," *Energies*, vol. 14, no. 17, 2021.
- [46] Gershenson, Naum I.; Ritzi, Robert W.; Dominic, David F.; Mehnert, Edward; Okwen, Roland T., "Capillary trapping of CO₂ in heterogeneous reservoirs during the injection period," *International Journal of Greenhouse Gas Control*, vol. 59, pp. 13-23, 2017.
- [47] Naum I. Gershenson, Robert W. Ritzi Jr., David F. Dominic, Edward Mehnert, and Roland T. Okwen, "Comparison of CO₂ Trapping in Highly Heterogeneous Reservoirs with Brooks-Corey and Van Genuchten Type Capillary Pressure Curves," *Advances in Water Resources*, vol. 96, pp. 225-236, 2016.
- [48] S. Bachu, "Drainage and imbibition CO₂/brine relative permeability curves at in situ conditions for sandstone formations in western Canada," *Energy Procedia*, vol. 37, p. 4428 – 4436, 2013.
- [49] D. Brant Bennion and Stefan Bachu, "Drainage and imbibition CO₂/brine relative permeability Relationships for Supercritical CO₂/brine and H₂S brine systems in

- intergranular Sandstone , Carbonate Shale and Anhydrite rocks," *SPE Reservoir Evaluation and Engineering*, 2008.
- [50] Yusuf Pamukcu, Suzanne Hurter, Laurent Jammes, Dat Vu-Hoang and Larry Pektot, "Characterizing and Predicting Short Term Performance for the In Salah Krechba Field CCS Joint Industry Project," *Energy Procedia*, vol. 4, pp. 3371-3378, 2011.
- [51] Yusuf Pamukcu, Suzanne Hurter, Peter Frykman, Fabian Moeller, "Dynamic Simulation and History Matching at Ketzin (CO₂SINK)," *Energy Procedia*, vol. 4, pp. 4433-4441, 2011.
- [52] Yousef Ghomian, Gary A. Pope, Kamy Sepehrnoori, "Reservoir simulation of CO₂ sequestration pilot in Frio brine formation, USA Gulf Coast," *Energy*, vol. 33, p. 1055–1067, 2008.
- [53] Idar Akervolla, Erik Lindeberga, Alf Lacknerb, "Feasibility of Reproduction of Stored CO₂ from the Utsira," *Energy Procedia*, vol. 1, p. 2557–2564, 2009.
- [54] Onoja, M. U. Shariatipour, S. M., "Assessing the impact of relative permeability and capillary heterogeneity on Darcy flow modelling of CO₂ storage in Utsira Formation," *Greenhouse Gases Science and Technology*, vol. 9, no. 6, pp. 1221-1246, 2019.
- [55] Seyyed Abolfazl Hosseini, Hamidreza Lashgari, Jong W. Choi, Jean-Philippe Nicot, Jiemin Lu, Susan D. Hovorka, "Static and dynamic reservoir modeling for geological CO₂ sequestration at Cranfield, Mississippi, U.S.A.," *International Journal of Greenhouse Gas Control*, vol. 18, pp. 449-462, 2013.
- [56] Jackson, S. J.; Krevor, S, "Small scale capillary heterogeneity linked to rapid plume migration during CO₂ storage.," *Geophysical Research Letters*, 2020.
- [57] S. J. Jackson, Q. Lin and S. Krevor, "Representative elementary volumes, hysteresis and heterogeneity in multiphase flow from the pore to continuum scale," *Water Resources Research*, vol. 56, no. 6, 2020.
- [58] Ronny Pini, Sally M. Benson, "Simultaneous determination of capillary pressure and relative permeability curves from core-flooding experiments with various fluid pairs," *Water Resources Research*, vol. 49, no. 6, pp. 3516-3530, 2013.
- [59] Raeesi, Behrooz; Morrow, Norman R.; Mason, Geoffrey, "Capillary Pressure Hysteresis Behavior of Three Sandstones Measured with a Multistep Outflow–Inflow Apparatus," *dose Zone Journal*, vol. 13, no. 3, pp. 0-11, 2014.
- [60] N.M. Burnside*, M. Naylor, "Review and implications of relative permeability of CO₂/brine systems and residual trapping of CO₂," *International Journal of Greenhouse Gas Control*, vol. 23, pp. 1-11, 2014.
- [61] Ji-Quan Shia, Ziqiu Xueb, Sevet Durucan, "Supercritical CO₂ core flooding and imbibition in Tako sandstone—Influence of sub-core scale heterogeneity," *International Journal of Greenhouse Gas Control*, vol. 5, pp. 75-87, 2011.
- [62] Richard L Christiansen, Susan M. Howarth , *Literature Review and Recommendation of Methods for Measuring Relative Permeability of Anhydrite from the Salado Formation at the Waste Isolation Pilot Plant*, California: United States Department of Energy, 1995.
- [63] Jean-Christophe Perrina, Michael Krause, Chia-Wei Kuo, Ljuba Miljkovic, Ethan Charob, and Sally M. Benson, "Core-scale experimental study of relative permeability properties of CO₂ and brine in reservoir rocks," *Energy Procedia* , vol. 1 , p. 3515–3522, 2009.
- [64] Rasoul Nazari Moghaddam, Mahmoud Jamiolahmady , *Steady State Relative Permeability*

Measurements of Tight and Shale Rocks Considering Capillary End Effect, Heriot-Watt University .

- [65] L. W. Lake, "Chapter 5 Multiphase Pore Fluid Distribution," in *Enhanced Oil Recovery* .
- [66] Ibrahim, M.N.; Koederitz, L.F., "Two-Phase Steady-State and Unsteady-State Relative Permeability Prediction Models," in *Proceedings of SPE Middle East Oil Show*, Bahrain, 2001.
- [67] Osoba, J.S., Richardson, J.G., Krever, J.K., Hafford, J.A. and Blair P.M., "Laboratory Measurements of Relative Permeability," *Trans. of the AIME. Petroleum Branch*, vol. 192, pp. 48-56, 1951.
- [68] Mingxing Bai, Lu Liu, Chengli Li, and Kaoping Song, "Relative Permeability Characteristics During Carbon Capture and Sequestration Process in Low-Permeable Reservoirs," *Materials(Basel)*, vol. 13, no. 4, 2020.
- [69] Honarpour, M. and S.M. Mahmood, "Relative-permeability measurements: An Overview," *Journal of Petroleum Technology*, vol. 40, no. 8, 1988.
- [70] Richard I. Christiansen, James S. Kalbus and Susan M. Howarth, "Evaluation of Methods for Measuring Relative Permeability of Anhydrite from Salado Formation: Sensitivity Analysis and Data Reduction," Sandia National Laboratories, 1997.
- [71] Naum I. Gershenzon, Mohamad Reza Soltanian, Robert W. Ritzi Jr., "Influence of small scale heterogeneity on CO₂ trapping processes in deep saline aquifers," *Energy Procedia*, vol. 59, p. 166 – 173, 2014.
- [72] Ehsan Saadatpoor; Steven L. Bryant; Kamy Sepehrnoori, "Effect of capillary heterogeneity on buoyant plumes: A new local trapping mechanism," *Energy Procedia*, vol. 1, no. 1, p. 3299–3306, 2009.
- [73] Zhao Hongjun, Liao Xinwei, Chen Yanfang and Zhao Xiaoliang, "Sensitivity analysis of CO₂ sequestration in saline aquifers," *Petroleum Science*, vol. 7, pp. 372-378, 2009.
- [74] B. Ülker, G. Pusch, F. May, "Numerical Analysis of Capillary Entrapment for Effective CO₂ Aquifer Storage," in *DGMK/ÖGEW-Frühjahrstagung*, Hannover, 2007.
- [75] E.J. Spiteri, R. Juanes, M.L. Blunt, and F.M. Orr Jr., "Relative Permeability Hysteresis: Trapping Models and Application to CO₂ Geological Sequestration," in *Annual Technical Conference and Exhibition*, Texas, 2005.
- [76] Bech, Niels; Frykman, Peter, "Trapping of buoyancy-driven CO₂ during imbibition," *International Journal of Greenhouse Gas Control*, vol. 78, pp. 48-61, 2018.
- [77] H. Alkan, Y. Cinar, and B. Ülker, "Impact of Capillary Pressure, Salinity and In-situ Conditions on CO₂ Injection into Saline Aquifers," *Transport in Porous Media*, vol. 84, no. 3, pp. 799-819, 2010.
- [78] Kumar, A.; Noh, M.; Pope, G.A.; Sepehrnoori, K.; Bryant, S.; Lake, L.W, "Reservoir Simulation of CO₂ Storage in Deep Saline Aquifers," in *Society of Petroleum Engineers SPE/DOE Symposium on Improved Oil Recovery - (2004.04.17-2004.04.21) Proceedings of SPE/DOE Symposium on Improved Oil Recovery*, Oklahoma, 2004.
- [79] Ana Mijic, Tara C. LaForce, Ann H. Muggeridge, "CO₂ injectivity in saline aquifers: The impact of non-Darcy flow, phase miscibility, and gas compressibility," *Water Resources*, vol. 50, no. 5, pp. 4163-4185, 2014.
- [80] G. C. Institute, "Global Status of CCS 2021," 2021.

- [81] R. Setså, "expronews.com," 2 December 2019. [Online]. Available: <https://expronews.com/technology/the-characteristics-of-a-co2-reservoir/>. [Accessed 01 June 2022].
- [82] Samuel C. M. Krevor, Ronny Pini, Lin Zuo, and Sally M. Benson, "Relative permeability and trapping of CO₂ and water in sandstone rocks at reservoir conditions," *Water Resources Research*, vol. 48, 2012.
- [83] Hailun Ni, Charlotte Garing, Sally M. Benson, "Predicting CO₂ Residual Trapping Ability Based on Experimental Petrophysical Properties for Different Sandstone Types," in *Greenhouse Gas Control Technologies*.
- [84] Xianmin Zhou, Fawaz Al-Otaibi and Sunil Koka, "Investigation of Relative Permeability Characteristics for Supercritical CO₂ Displacing Water and Remaining Oil after Seawater Flooding in Carbonate Rocks at Reservoir Conditions," in *SPE Middle East Oil & Gas Show and Conference*, Manama, 2017.